Nanomechanical Sensors: Analyzing Effects of Laser-Nanowire Interaction and
Electrodeposited Clamps on Resonance Spectra


by


Fan Weng
B.Sc., Beihang University, 2013

A Thesis Submitted in Partial Fulfillment
of the Requirements for the Degree of

MASTER OF APPLIED SCIENCE

in the Department of Mechanical Engineering

# Supervisory Committee

Nanomechanical Sensor: Analyzing Effects of Laser-Nanowire Interaction and
Electrodeposited Clamps on Resonance Spectra

by

Fan Weng
B.Sc., Beihang University, 2013

**Supervisory Committee**

Dr. Rustom Bhiladvala, Supervisor
(Department of Mechanical Engineering)

Dr. Colin Bradley, Departmental Member
(Department of Mechanical Engineering)

# Abstract

**Supervisory Committee**

Dr. Rustom Bhiladvala, Supervisor
(Department of Mechanical Engineering)

Dr. Colin Bradley, Departmental Member
(Department of Mechanical Engineering)

This thesis presents work to help enable the transition of sensitive nanoscale instruments from research laboratory demonstration to societal use. It focuses on nanomechanical resonators made by field-directed assembly, with contributions to understanding effects of materials, clamp geometries and laser measurement of motion, towards their use as commercial scientific instruments.

Nanomechanical resonators in their simplest form are cantilevered or doubly-clamped nanowires or nanotubes made to vibrate near one of their resonant frequencies. Their small mass and high frequency enable extraordinary mass sensitivity, as shown in published laboratory-scale demonstrations of their use for detection of a few molecules of prostate cancer biomarker and of their response to mass equal to that of a single proton. However such sensitive devices have been prohibitively expensive for societal use, since the fabrication process cost scales with number of devices and the chip area covered, when they are made using standard electron beam lithography. Our laboratory has published new results for the method of field-directed assembly, in which the nanofabrication process cost is independent of the number of devices. While drastically lowering the cost, this method also broadens the range of device materials and properties that can be used in instrument applications for sensitive mass and force detection. Unanswered questions affecting the performance of devices made by this method are studied in this thesis.

Clamping variability can cause uncertainties in the device resonant frequency (effective stiffness), raising manufacturing metrology costs to track reduced homogeneity in performance. Using a numerical model, we quantify how compliant clamp material and insufficient clamp depth reduce the effective stiffness and resonance frequency. Obliquely clamped nanowires and defects at the clamp-nanowire interface break the symmetry and split the resonance frequency into fast and slow modes. The difference of resonance frequency between the fast and slow modes corresponds to the degree of asymmetry and must be controlled in fabrication to keep device error bounded.

Optical transduction has been used for measuring the nanoresonator frequency spectrum; however, the influence of the laser in the measurement process is only recently receiving attention and is not well understood. We found that the measured spectrum is significantly influenced by laser-nanowire interaction. Variation of input laser power could result in resonance peak shifts in the kHz range for a resonance frequency in the MHz range, which could reduce device mass resolution by a factor of 100 or greater. As the laser power is increased, the resonance frequency decreases. The heating effect of the laser on temperature-dependent Young's modulus could explain this phenomenon. To our surprise, we also found that the amplitude and frequency of the resonance peak signal vary significantly with the angle made by the plane of laser polarization with the nanowire axis. Our measurements established that the maximum signal amplitude is seen when the plane of the linearly polarized laser is parallel to SiNW or perpendicular to RhNW. Maximum resonance frequency was found when laser is polarized perpendicular to SiNW or parallel to RhNW.

# Table of Contents

# List of Tables

# List of Figures

# Acknowledgments

*I would like to thank:*

# Dedication

To my beloved parents: Weijun and Shujun

# Chapter 1

# Introduction

Nanowires are solid, rod-like structures with diameters up to a few hundred nanometers and are commonly considered as one-dimensional nanoscale structures. The last decade of research on nanowires has greatly extended the boundary of possible applications. The geometry and materials of nanowire have been chosen to make them core building blocks of optoelectronic devices such as solar cells [1 - 3], photodetectors [4 - 5] and lasers [6, 7]. The study of field effect of semiconductor nanowires [8, 9] opens a door to their application to chemical [10, 11] and biological sensing [12 - 15]. In energy harvesting applications, piezoelectric nanowires also show excellent performance [16].

In addition to nanowire devices based on unique electrical and optical behavior, nanowire resonators are based on the mechanical properties of nanowires. In fact, nanowire resonators can be shaped to serve as a testbed for mechanical property measurement of one-dimensional nanostructures. Very limited literature exists on investigation of artifacts arising from the transduction method, especially for optical transduction. These artifacts can significantly influence the resonance frequency signal although numerous reports of application of high sensitivity do not discuss them. Besides transduction, there is also little research on how the clamp condition can change resonance frequency of cantilevered nanowire resonators. In this thesis, results of work with nanowire-based cantilevered resonators are presented for both silicon nanowires (SiNW) and rhodium nanowires (RhNW). Details of nanowire synthesis and fabrication of nanowire resonator chip will not be covered. The effect of fabricated clamp condition of nanowire resonator is addressed with simulation results of the resonance frequency.

The optical transduction method employed in this thesis is used to measure the resonance spectrum of the nanowire mechanical resonator. The plane of polarization and the power of the probing laser beam are shown to have significant impact on the amplitude and peak frequency of the measured spectrum.

## 1.1    Nanowire Mechanical Resonators

### 1.1.1  Architecture and Sensitivity

A nanomechanical resonator is a nanoelectromechanical systems (NEMS) device constructed from nanoscale components, vibrating around one of its resonance frequencies [17]. Nanomechanical resonators can have a variety of shapes, e.g. rectangular cross-section beam [18, 19], hollow tube [20, 21], rod [22, 23], and even a complex structure like a nanowire lattice [24]. To simplify, all mentioned "nanowire resonators" in this thesis refer to mechanical resonators made from a single nanowire. The resonance frequency depends on the mass of nanowire, and generally speaking, decreases as the mass increases. This distinctive feature is of interest to both scientific and industrial sectors and intriguing nanowire resonator applications have been introduced in the last decade. In the physics community, nanowire resonators are widely used in studying the quantum behavior of mechanical structure [25]. In biosensing, nanowire resonators exhibit the capability of detecting the mass of a few biomarker molecules to enable early stage diagnosis of disease [26]. Also, mechanical nanoresonators can be designed for material property measurement of 1D nanostructures [27].

The mass sensitivity of a nanomechanical beam resonator ($\Delta f /\Delta m$) relies on the ratio of its peak resonance frequency ($f$) to its mass ($m$). For a cylindrical beam resonator of length $L$ and diameter $D$, with any fixed value of aspect ratio, the mass sensitivity ($\Delta f /\Delta m$) $\sim D^{-4}$, hence decreasing beam diameter from 1 μm to 0.1 μm, increases the mass sensitivity by four orders of magnitude [28, 29]. A recent experiment has shown an extraordinary mass sensing resolution of 1.7 yoctogram, which is comparable to the mass of a single proton (1.673E-24 g) [30]. Moreover, small dimensions enable reducing raw

material cost in terms of mass production after commercialization of the nanomechanical resonator sensors.

## 1.1.2 Actuation Methods

Three widely used actuation methods in the MEMS and NEMS community are introduced in this section: magnetomotive, electrostatic and piezoelectric techniques. However, other well-established actuation methods such as thermal actuation and magnetostrictive actuation have also been used in exciting the vibration of nanomechanical devices [31].

The Lorentz force law shows that a force will be applied to moving charge in an electromagnetic field. The magnetomotive method is based on the Lorentz force. A doubly clamped nanobeam resonator is placed in a magnetic field with high intensity [32], requiring, in some cases, a superconducting solenoid [33]. An AC signal applied to the two ends of the nanobeam produces AC current flows through the beam. The resulting Lorentz force actuates nanobeam vibration in-plane or out-of-plane, depending on the angle between the axis of nanobeam and the magnetic field vector. Magnetomotive actuation has a broad operation bandwidth. Detection of NEMS fundamental frequency in microwave range (GHz) where parasitic impedances would overwhelm other methods, has been reported [34]. However, dependence on an intense magnetic field (several Tesla) makes magnetomotive actuation less favorable considering the power requirement (superconducting coil) or device size (large permanent magnet).

Piezo actuation uses the reverse piezoelectric effect – material generates stress in response to the external electric voltage applied. Under an alternating current (AC) signal of chosen frequency, the piezoelectric material will squeeze and expand its geometry with corresponding frequency, providing the vibration force. Depending on whether the piezoelectric material is part of the nanomechanical resonator, piezo actuation can be divided into two categories: direct actuation and indirect actuation. In direct piezo actuation, the piezoelectric material is integrated with the nanomechanical resonator, and as a result, the resonator fluctuates with the input AC voltage [35, 36]. Where the nanoresonator does not incorporate piezoelectric materials, the piezo actuator is bonded

with the chip having mounted resonator devices so that the two move together [37]; this is the indirect method. Direct excitation technique obviously wins from the point of view of driving efficiency but it cannot be used to investigate nanoresonators of all materials. Resonance frequency measurements in this thesis exploit the indirect piezo actuation method using a commercial piezo disk (as shown in Section 3.3).

Electrostatic (or capacitive) actuation scheme could have been considered in this thesis project as well, but has not these experiments. The basic structure of the electrostatic actuator resembles a two-plate capacitor, an elastic conductive resonator suspended above a flat counter electrode [38]. Applying AC voltage to the actuator imposes a variation of charge on both conductors. Therefore, the electrostatic force as a result of attraction between positive and negative charges changes with the AC frequency. Capacitive actuation method works well in MHz range [39] but parasitic capacitance impedes its usage in the GHz frequency range [31].

## 1.1.3 Motion Transduction Methods

Nanomechanical resonators feature very small size and high resonance frequency, enabling high mass resolution applications to small molecule and other mass detection. Their sub-micrometer size and MHz to GHz range frequency make measurement of the motion is much more demanding. Presently available measurement techniques are introduced in this section, such as amplitude measurement by scanning electron microscopy (SEM), optical transduction, and magnetomotive and capacitance modulation methods.

SEM images with rastering time greatly exceeding the sub-microsecond time period of the resonator, have been used to visualize resonance of nanoscale structures for over a decade [40 - 42]. The boundaries of motion of the vibrating nanostructure can be recorded in an SEM image when AC actuation approaches the natural resonance frequency. This is a clear and direct method, but one which is time-consuming and allows a relatively small number of spectral data points. The displacement amplitude of the nanowire as a function of frequency is obtained from SEM images. As mentioned in Section 1.1.2, magnetomotive actuation benefits from Lorentz force in a static magnetic

field and in turn, electromotive force (EMF) is induced by the motion of conducting nanobeam [33]. The fluctuation of EMF can be detected by the analyzing circuit. Measurement of very-high-frequency (VHF) NEMS devices have been published using magnetomotive transduction method with the help of radio frequency (RF) reflectometry technique [43]. Capacitive read-out is based on the capacitance change brought by spacing change between two parallel conductors. The amount of capacitance change of a MEMS system is usually in pF range which is comparable to the influence value of parasitic capacitance [29]. CMOS circuit integration with the resonator device radically relives the effect of parasitic capacitance in capacitive transduction, enabling approximately 17ag/Hz mass resolution [44].

Optical transduction is also commonly used to detect the motion of nanomechanical resonator. Path-stabilized Michelson interferometry and Fabry-Perot interferometry are two setups enabling high sensitivity and broad bandwidth [45]. Detailed description of the optical transduction method used in this thesis work is written in Section 4.1. The operation relies on the mechanism that the dimension of the optical cavity and the reflectivity are correlated [46], which means the intensity of the reflected laser beam varies with the vibration of nanoresonator, since height between nanostructure and reflecting pad underneath is varying.

## 1.1.4 Field-directed Assembly

Top-down methods are the first choice to create microscale structure by patterning and etching from a larger bulk of material, but the presence of undercuts, regions of etched sacrificial layer under the support, in top-down methods increases the compliance of structure introducing energy loss and cross talk [17, 47]. The etching process used to suspend the beams can give rise to distortion for cantilevered structures, or induce tension-dependent string-like vibration modes in doubly-clamped structures [17, 48]. Field-directed assembly, enabling a large number of devices to be made over large area, without the prohibitive cost of electron beam lithography, is a cost-effective bottom-up method for large area fabrication of nanostructure (see Figure 1.1) that can solve top-down limitations mentioned above. Synthesized nanoscale structures under the

control of field forces, can be positioned at pre-patterned locations to form a desired nanostructure system [49]. Field-directed assembly targets decreasing fabrication cost and enables manipulating nanowires made of different shapes and materials. It allows functionalization (e.g. for biosensing) to be done off-chip, making multiplexing possible for a chip nanosensor platform. Despite these advantages, new problems and questions of field-directed assembly method need to be examined. Clamping rigidity is one of the causes of deviations of the resonance frequency from theoretical value. Field-directed assembly also currently allows less control on clamping angle and clamped depth of nanowire resonator, reducing the repeatability of fabrication compared to the top-down methods.



Fab-6 1.0kV 8.8mm x600 SE(M) 11/5/2013                    50.0um
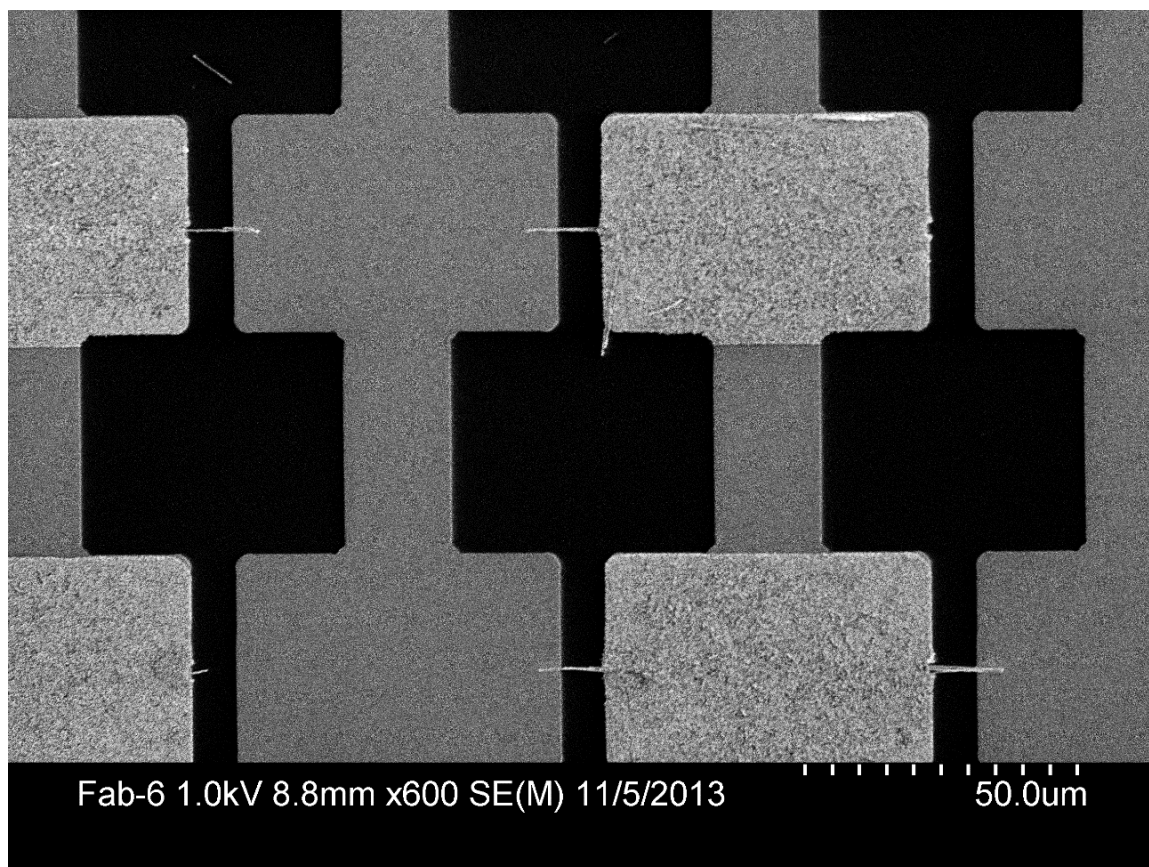
**Figure 1.1** SEM image of nanoresonator arrays fabricated by field-directed assembly method.

## 1.2    Research Objectives

The long-term research goals of our Nanoscale Transport, Mechanics & Material Lab (NTMML) is to enable robust fabrication and highly-sensitive transduction methods for nanoscale sensors at a reasonable cost. This thesis research work is driven by the desire to obtain sensitive and accurate measurements with nanowire resonators, which requires an understanding of the factors influencing optical transduction signals and the effect of nanowire resonator structure on resonance frequency. Both areas of knowledge would be valuable for conducting an accurate resonance measurement as well as guiding effective fabrication of nanowire resonators, to help push the nanowire resonator devices forward towards commercial applications.

Resonance frequency calculation of a cantilever beam from theory is made with some restrictive assumptions, such as rigid clamping, uniform geometry and perpendicular orientation to the clamp wall. In actual fabrication of nanowire resonators, none of these conditions can be perfectly achieved causing a resulting resonance frequency departure from theoretical calculation. The coupling between nanowire resonator fabrication steps and its resonance frequency makes it important to understand the synthesis of single nanowires and the fabrication of nanowire devices. The clamp condition is of particular interest to this thesis work due to its direct effect on nanowire resonance frequency. Finite element analysis of nanowire resonator helps in studying the resonance frequency under various clamp conditions. Depth, material, angle and defects of the clamping block are evaluated in terms of their influence on nanowire resonance frequency.

Optical transduction has often been used to measure the spectrum of nanomechanical resonators. However, the optomechanics community does not yet have conclusive explanations for the interaction between the probing laser and nanoresonator. The signal amplitude of the resonance frequency peak depends strongly on the scattered light power from nanowire resonator and counter electrode below it. The angle of the plane of polarization of the laser with respect to the axis of nanowire resonator, should be studied for its effect on signal amplitude. The heating effect of the probing laser is often omitted by researchers. This may be inappropriate for nanoscale resonators. The resonance

frequency shift induced by laser bolometric effect matters since its magnitude is comparable to the mass sensing scale. Thus an experiment on input laser power also should be performed to prove its correlation with resonance frequency. Two kinds of nanowire resonators made of silicon nanowire (SiNW) and rhodium nanowire (RhNW) are investigated in the research. This work reveals some answers to the light-nanowire coupling effect which is benefit for interpreting resonance frequency signal of optical transduction method.

## 1.3    Thesis Structure

Following this chapter, resonance frequency simulation for nanoresonators is presented, considering a variety of clamping conditions. This is followed by a thorough introduction to the optical transduction setup and interprets the center peak frequency and quality factor of resonance spectrum. Light-nanowire interaction is then demonstrated with a study of the effect of plane of laser polarization and laser input power on both silicon and rhodium nanowire. Conclusion and suggestions for future work can be found at the end of each chapter. The contents of each of the following chapters are summarized below.

Chapter 2 focuses on the effect of clamping conditions on the resonance frequency of cantilevered nanowire resonator. 3D COMSOL simulation of a nanowire resonator is demonstrated. This chapter presents the simulations results of clamp depth, clamp material, angle of clamping and defects at clamping area.

Chapter 3 is a description of optical transduction method and resonance signal spectrum. Piezo disk and electrostatic actuation methods are integrated in one frame inside test vacuum chamber. Details of optical detection method are illustrated with optical components and electronic devices. General information of single rhodium nanowire synthesis and nanowire resonator chip fabrication is introduced in this chapter. The fundamental resonance frequency and quality factor are two characteristic parameters of a nanowire resonator. They are interpreted with actual nanowire resonator measurement results.

Chapter 4 presents the interaction between probing laser states and nanowire resonator. The phenomenon that changing of the plane of polarization of the laser results

in the variation of resonance peak amplitude is observed for both silicon and rhodium nanowire. The shift of resonance frequency is explained by the varying injected laser power.

Chapter 5 reviews the main conclusions of this M.A.Sc. thesis.

# Chapter 2

# Clamp Effect on Resonance Frequency

Understanding mechanical properties, e.g. Young's modulus, in micro/nanoscale is of particular importance to predict nanoelectromechanical system performance [27]. Before Poncharal and co-workers introduced resonance excitation based technique, Young's modulus was mainly determined by rigidity measurement for micro/nanoscale beams [50]. Euler-Bernoulli beam theory [51] gives the $n$th mode resonance frequency of a uniform cantilevered beam as

$$f_n = \frac{\beta_n^2}{2\pi}\sqrt{\frac{EI}{mL^4}}$$
(2.1)

where $E$ is the Young's modulus of beam, $I$ is beam cross-section moment of inertia, $m$ is the mass per unit length and $L$ is the length of beam. $\beta_n$ is the eigenvalue derived from the characteristic equation $\cosh(\beta_n)\cos(\beta_n) = -1$. The eigenvalues of the first three modes are $\beta_0 = 1.875$, $\beta_1 = 4.694$, $\beta_2 = 7.855$, and a close approximation to eigenvalues for the higher modes is given by

$$\beta_n \approx (n - \frac{1}{2})\pi$$
(2.2)

By measuring the resonance frequency of the beam and determining the beam geometries, Young's modulus can be calculated from Equation 2.1. This method has been widely used to determine Young's modulus of nanowires [40], [52]. However, the calculated value usually deviates from the true value because of many non-ideal configurations [53], for example, non-ideal clamp, non-straight wire, coating layer. Equation 2.1 is derived using a fixed boundary condition at one end of the beam where

displacement and slope are zero. It is called "rigidly" or "perfectly" clamped. But every real clamp will have some deviation from rigid behavior, depending on its material, dimensions and uniformity of contact with the nanowire. To study the extent of that deviation, we describe, in this chapter, numerical simulation results of the influence of different clamp conditions on the resonance frequency of nanowire resonator. We consider following configurations in the simulation: 1) depth of nanowire clamped; 2) material of clamp; 3) angle of nanowire axis with respect to the normal to the clamp wall and 4) defects at clamp nanowire interface. The finite element package COMSOL was validated against analytic solutions and used in these simulations.

## 2.1   COMSOL Model of Nanowire Resonator

COMSOL Multiphysics is a widely-used finite element analysis software package for many applications in physics and engineering. Nanowire resonator model is created and its eigenfrequencies are calculated using the 3D Solid Mechanics module. The basic structure of the modeled clamp (see Figure 2.1) incorporates a block (clamp) with a cylindrical hole where the rod will be clamped and a solid cylindrical rod (the nanowire) inserted into the very end of the hole. The length of nanowire in the model is defined as the portion that is suspended outside the clamp. The material and geometry assigned to the clamp and nanowire were varied to simulate clamp conditions studied.
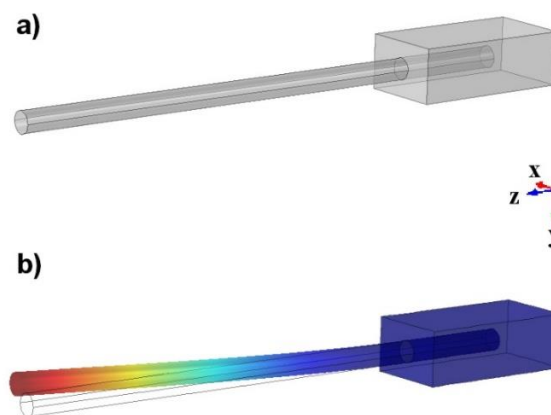


**Figure 2.1** a) Three-dimensional model of the clamp for a nanowire resonator in COMSOL simulation. b) Simulation result representing displacement of each part of nanowire resonator with colors.

The bottom surface of the clamp block is given the fixed constraint condition (displacement $u = 0$, slope $du/dx = 0$) while the rest of the clamp block and nanowire are free. This boundary condition reflects the fact that the bottom surface of the clamp attaches to the substrate on chip on which the nanowires and clamps are mounted. Here, the assumption that the nanowire does not slip with the respect to the clamp material, is used. The meshing process discretizes the 3D model into a large number of elements with predefined "extra fine" size. The eigenvalue Solver Algorithm computes the eigenfrequencies of the model in the final step.

## 2.2　Simulation Results and Discussion

### 2.2.1　Comparison to Theoretical Resonance Frequency

Euler-Bernoulli beam theory [51] yields the result shown in Equation 3.1, from which the resonance frequencies of a uniform cylindrical beam with one end fixed by a rigid clamp can be theoretically calculated as

$$f_n = \frac{\beta_n^2}{8\pi}\sqrt{\frac{E}{\rho}}\frac{D}{L^2} \tag{2.3}$$

where $D$ is the beam diameter, $L$ is the length, $E$ is the Young's Modulus and $\rho$ is the density of beam material, $n$ is the mode number. Resonance frequency $f$ is proportional to $\beta_n^2\sqrt{E}$. In the material property test, we want to measure $E$, which can vary with crystallite size, orientation, or crystal direction in single-crystal nanowires. For example, gold can have 44/88/117 GPa Young's modulus values for crystal directions (100), (110) and (111), respectively. $\beta_n$ can vary with clamp's departure from perfect rigidity. This chapter presents numerical simulation results to evaluate the resonance frequency dependency on clamp rigidity and imperfection.

The fundamental resonance frequency $f_0$ from simulation of the nanowire resonator is based on the clamp model introduced in Figure 2.1. Nanowire length and diameter are two variables. Dimension of clamp is $1.5\mu m \times 1.5\mu m \times 3\mu m$. The clamp material is

silver with a Young's modulus of 83GPa and a density of 10,490kg/m³. The nanowire material is rhodium and its properties are shown in Table 2-1.

**Table 2-1** Mechanical Properties of Five Clamping Materials

| Clamping materials | Diamond | Rh | Cu | Ag | Au |
|---|---|---|---|---|---|
| Young's Modulus (GPa) | 1,220 | 275 | 130 | 83 | 78 |
| Poisson Ratio | 0.2 | 0.26 | 0.34 | 0.37 | 0.44 |
| Density (kg/m³) | 3,520 | 12,450 | 8,920 | 10,490 | 19,300 |

(Mechanical property data uses the built-in library of COMSOL)
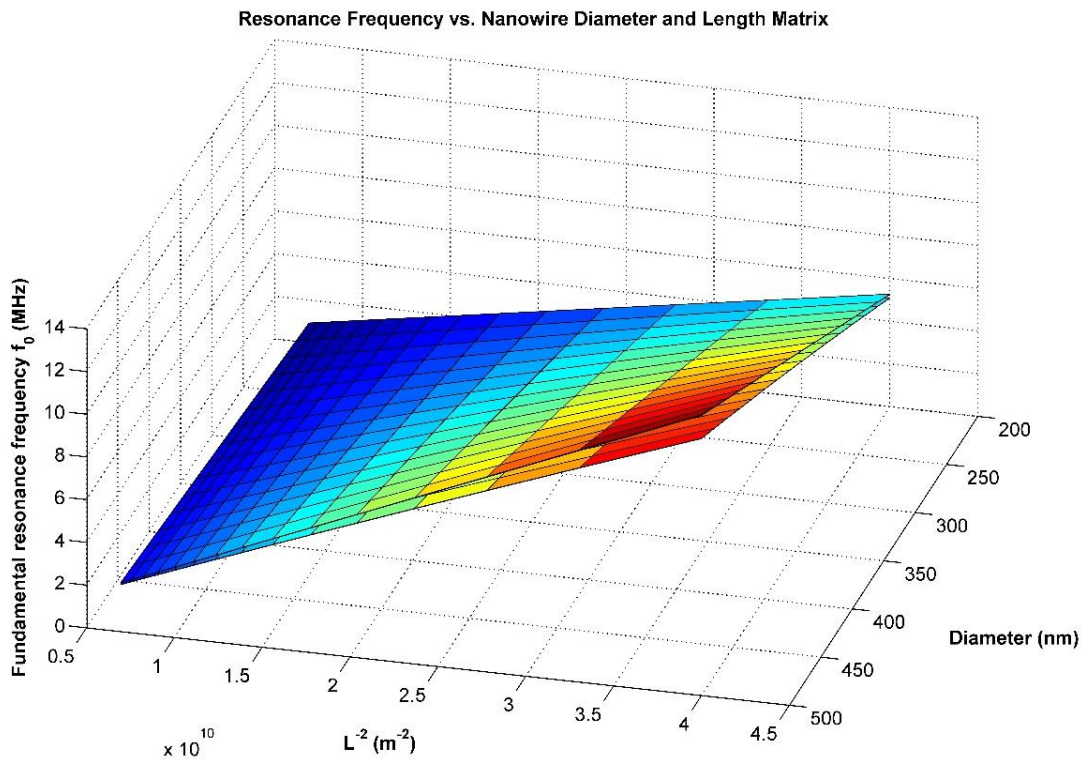


**Figure 2.2** 3D surface plot of nanowire resonance frequency as a function of nanowire diameter and length. The strongest deviation between the theoretical solution (upper surface) and clamp model simulation (lower surface) in the figure occurs at shorter nanowire length and larger diameter.

Figure 2.2 displays the theoretical resonance frequencies calculated by Equation 2.3 (upper surface plot) and simulated results using clamp model (lower surface plot) with the nanowire geometry matrix $[D, L^{-2}]$ as a 3D plot view. In both the theoretical and clamp model, resonance frequencies linearly increase with an increase of $D$ and $L^{-2}$. But the gap between the upper and lower planes becomes wider correspondingly and clamp

model resonance frequency is always less than the theoretical one. This deviation suggests that the clamp conditions, such as clamped depth, clamp material and clamp morphology, might present influence on resonance frequency departing from rigidly clamped condition.

## 2.2.2 Effect of Clamped Depth

Imagine a scenario, where a finger presses one end of a pencil on the table surface with the remainder of the pencil hanging off the edge. If the pressed part of the pencil becomes shorter, the finger would need to apply more force to keep the rest of the pencil suspended. This variant of leverage effect might be found in a clamped nanowire resonator as well, since clamp depth acts similarly. Three rhodium (Rh) nanowire resonators were simulated with the same diameter of 400nm but different lengths (6μm, 8μm, 12μm) using silver clamp model (Figure 2.1). Relevant material properties of silver as the clamp material are listed in Table 2-1. The dimensions of the clamp are $1.5 \mu m \times 1 \mu m \times 3 \mu m$.

It is shown in Figure 2.3 that the deviation of fundamental resonance frequency of nanowire resonators from theoretical value reaches a constant (defined as "plateau deviation") when clamp depth exceeds 0.8μm (blue vertical line in Figure 2.3). But if clamp depth goes below that threshold value, the resonance frequency deviations dramatically escalate (defined as "extreme deviation"). We define that threshold value as "minimum required clamped depth"; clamp depths below this value represent avoidable reductions from the theoretical resonance frequency. For shorter nanowire, both plateau deviation and extreme deviation are more significant than those longer nanowires as seen in Figure 2.3. Large error would exist if clamped depth is very short when Young's modulus is deduced from nanowire resonator resonance frequency using Equation 2.3. It should be noted that large increase in clamped depth, above the minimum required, will not make the resonance frequency any closer to the theoretical values, since clamp material also affects it. This will be discussed in Section 2.2.3.

**Deviation from Theoretical Resonance Frequency**
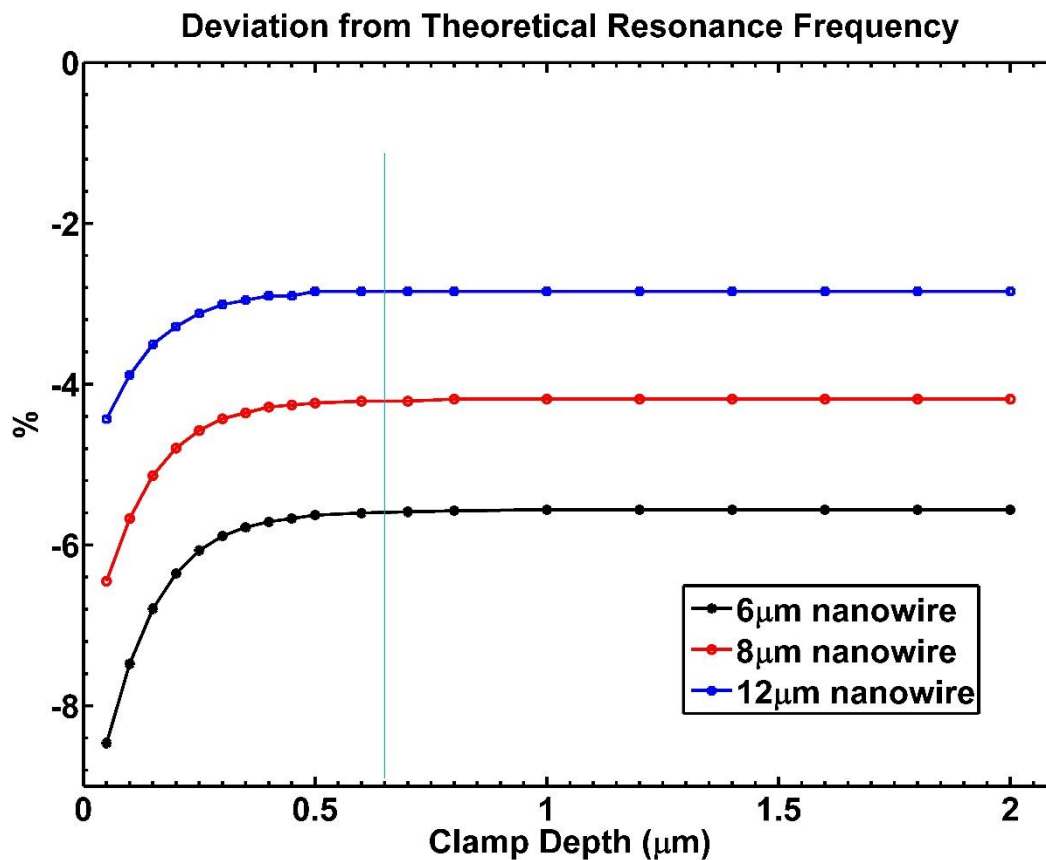


**Figure 2.3** Plot showing percentage of deviation predicted by clamp model simulation, with respect to theoretical results. For the same nanowire length, for shorter clamped depths, there is a larger deviation from the theoretical resonance frequency. Beyond a threshold value of clamp depth the deviation will reach a plateau. The figure shows the plateau resonance frequencies of 12μm nanowire is closest to the theoretical calculation, while the stiffer 6μm nanowire plateau shows the largest gap from the theoretical value.

Qin et al. have reported a similar clamp size influence on cantilevered ZnO nanowire resonance frequency [54]. As they increase the deposited clamp width on the one end of ZnO nanowire on a tungsten probe, the resonance frequency increases approaching the theoretical result under rigidly clamped condition. Our work on clamped depth as well as their research indicates that if cantilevered nanowire resonator is used to measure Young's modulus, a large enough clamped depth could minimize the error.

## 2.2.3 Variation of Mode Constant $\beta_n$ with Clamping Material Properties

The clamp material has an impact on the constraint of the clamped end. Therefore, different material properties could introduce different magnitudes of deviation from the theoretical resonance frequency of the nanowire resonator. In the clamp model simulation, diamond [55], rhodium, copper, silver and gold are selected as clamp materials. The clamp model is for a Rh nanowire (diameter = 400nm, clamp depth = 2μm) and a clamp block ($1.5\mu m \times 1\mu m \times 3\mu m$). By investigating five clamp materials with parameters shown in Table 2-1, the percentage of deviation of resonance frequency from the theoretical value for a rigid clamp is plotted in Figure 2.4.

It is clear from the result, using the same nanowire and clamp dimensions, the clamp material with highest stiffness (larger Young's Modulus value) yields a lower resonance frequency deviation from the theoretical calculation. For a Rh nanowire resonator longer than 6μm, the diamond clamp drives resonance frequency less than 2% below theoretical value, which shows it is the material having the least change in resonance frequency. The material showing the highest change of resonance frequency in the simulation is gold, yielding 4.4% more deviation than diamond clamp for a 5μm-long Rh nanowire. However, such discrepancy reduces to 1.5% as the length of nanowire resonator is extended to 15μm. The resonance frequency gap between clamp model and theoretical results shrinks with the increment of nanowire resonator's length for all kinds of clamp materials, which corresponds to the discussion in Section 2.2.1. Silver and gold are commonly picked for electrodeposition of clamp. Their resulting resonance frequency deviations from the theoretical records are almost undistinguishable. But considering the purchasing price perspective, silver would be a better candidate for clamp material, with the same effect on resonance frequency, but with a lower cost compared to gold. Murphy et al. [56] have determined that the stiffness of electron-beam induced deposition clamps influence the nanowire mechanical response in MEMS-based tensile testing. Since the clamp material is compliant, the actual boundary condition is neither rigidly clamped nor completely free causing the resonance frequency to be in between these limits. Ruoff's

group put forward a beam-embedded-in-an-elastic-foundation model to obtain the resonance frequency of nanowire taking clamp material effect into account [57].
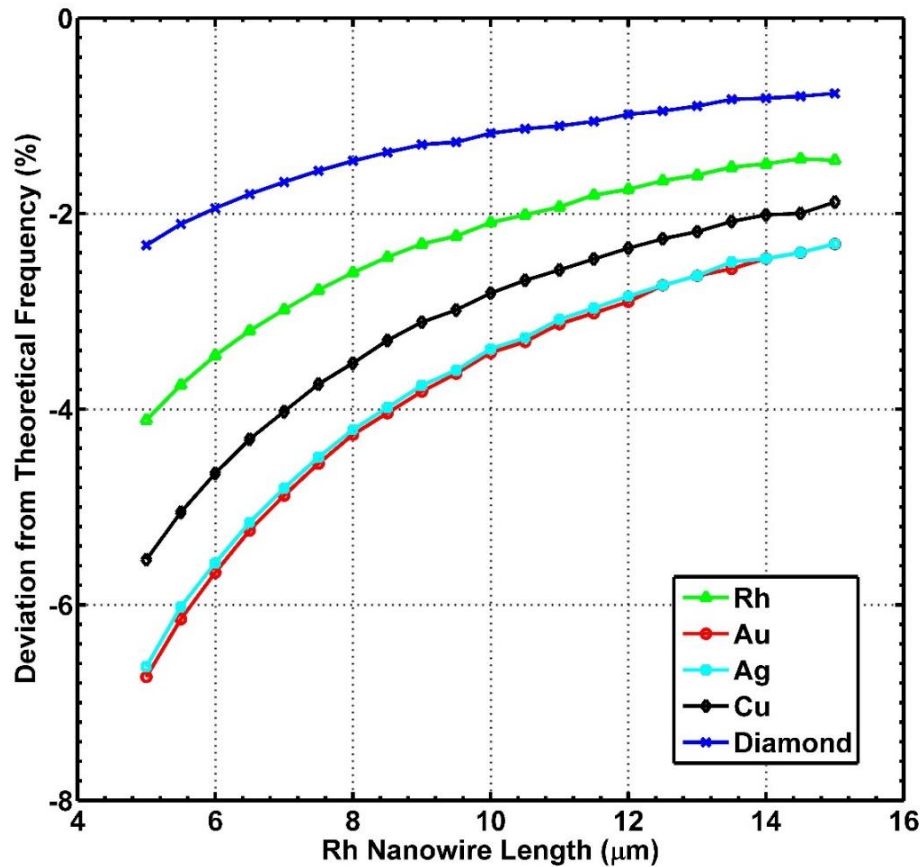


**Figure 2.4** Simulation results of resonance frequency deviation from theoretical values versus nanowire length for five clamp materials. The length of the nanowires is varied from 5μm to 15μm; the diameter is 400nm and clamp depth is 2μm. The diamond clamp, with highest Young's modulus and lowest Poisson Ratio, shows the least resonance frequency deviation from the ideal situation. Effects of gold and silver clamps on resonance frequency are similar. For all the materials, with increase in the nanowire length, resonance frequency tends to approach the ideal result.

To study which material property matters to resonance frequency, simulation was done on a nanowire with a length of 8μm, diameter of 400nm and clamped depth of 2μm. Results showed that Young's modulus is the most important property to influence resonance frequency (see Figure 2.5a). With Poisson's ratio of 0.44 and density of 19,300 kg/m$^3$, the resonance frequency increases about 9% when changing Young's modulus

from 10 to 1000GPa. Further, increasing Young's modulus makes resonance frequency approach the theoretical value, 4.11MHz. Based on these resonance frequency results and Equation 2.3, effective $\beta_n$ is calculated and plotted in Figure 2.5b.
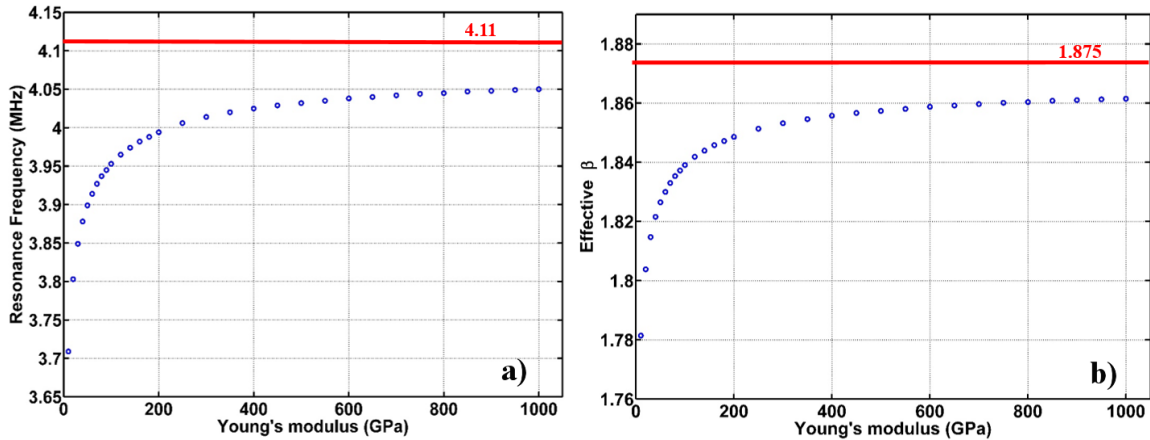


**Figure 2.5** a) Resonance frequency as a function of Young's modulus of clamp material; b) Effective $\beta_n$ as a function of Young's modulus calculated from the resonance frequency values in plot a). As the increase of Young's modulus, $\beta_n$ gradually approaches the theoretical value 1.875.

## 2.2.4  Two Vibration Modes Induced by Clamped Angle and Clamping Defects

Field-directed assembly as one of the most promising bottom-up methods to manufacture NEMS devices at a low cost is under intensive study and recent research has presented a framework with clamped nanowire device yields of 88% available sites [49]. However, all nanowires counted in this high yield figure will not have the nanowire clamped in perfect conditions. One common problem is when positioning nanowire on the clamping site, there is a significant chance that nanowire axis is not perpendicularly aligned with the clamp site wall. This gives rise to a clamp-related phenomenon that does not occur with nanobeams made by top-down methods. In this section, a simulation model is used to study the oblique clamped angle influence on the resonance frequency.

The Rh nanowire in the model is 8μm long, 400nm width and 2μm clamp depth. Clamp material was chosen to be gold and the angle $\delta$ is the variable representing the angle between nanowire axis and perpendicular line to the clamp wall. Note that the

clamping angle is considered in the yz plane, no other out-of-plane oblique clamping is included in the discussion.
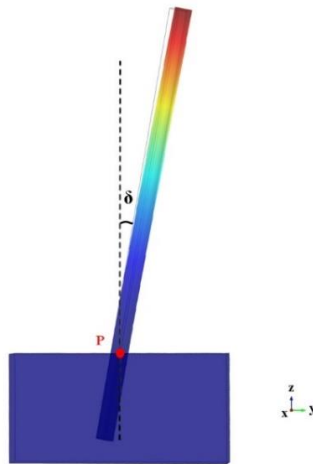


**Figure 2.6** Illustration of oblique clamped nanowire resonator model. Nanowire clamped length and free length are both held constant. Clamped angle $\delta$ is varied from 0 ° to 45 °, achieved by rotating the rest position, in steps, about point *P*.
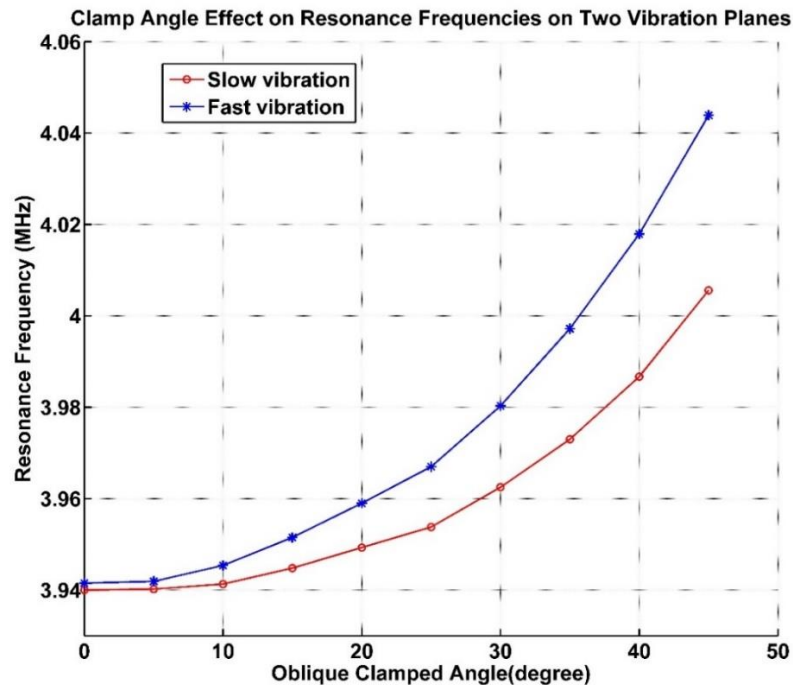


**Figure 2.7** Resonance frequencies of two vibration modes for different clamped angles. Symmetry of two vibration modes is reduced with the increase of clamped angle as shown. The final asymmetry approaches 40kHz resonance frequency difference between fast and slow vibration modes, at 45 °.

Any nanowire resonator vibration can be broken into two orthogonally vibrating planes, xz and yz planes in Figure 2.6. In an ideally symmetric situation, the resonance frequencies in these two planes should be the same. Since perfect symmetry is impossible to achieve, resonance frequencies in two planes always have a difference and the two vibration modes are then defined as fast mode and slow mode depending on the value of resonance frequencies they have. When the nanowire is normally clamped ($\delta = 0$), two vibration modes have almost identical resonance frequency. But as $\delta$ increases, the symmetry is gradually destroyed, with resonance frequency difference between fast and slow modes increasing. At $45°$ clamped angle, resonance frequency of fast mode is ~40kHz higher than the slow mode (see Figure 2.7). Usually, in optical measurement of nanowire resonance frequency, a single resonance peak will be detected on the spectrum analyzer. But frequency divergence of the two vibration modes could show two resonance peaks on spectrum analyzer, with frequency difference much lower than the frequency difference of with respect to nearest resonant modes.

Clamping defects are unfilled regions around the clamp-nanowire interface that could be left during the clamp electrodeposition process. The existence of these empty spaces allows the nanowire at the interface to move with partial restriction by the clamp material. For this, a 3D model of nanowire resonator featuring a cylindrical tube replacing the block clamp is used in sections above. A sector on the clamping cylinder is removed to mimic the defect, which consistently has the same length and clamp depth through the simulation. The size of defect is determined by the opening angle $\theta$ depicting in the zooming-in inset of Figure 2.8. To increase the defect size we simply widen the opening angle. In the cylinder tube model simulation, constant parameters are: nanowire length of 8μm, diameter of 400nm, clamp depth is 2μm, clamping tube has an inner diameter of 400nm, outer diameter of 800nm and length of 3μm. The outer surface of clamp tube is specified as being rigidly fixed.

The resonance frequency of two vibration planes should be equivalent for perfect clamping condition because of symmetric nanowire and clamping. The introduction of a defect on the clamping area breaks the symmetry and the void space and defect sets that part of the nanowire boundary free from the constraint of clamping material. This boundary condition reduces the resonance frequency in the vibration plane centered

within the defect location. Hence, two vibration frequencies diverge, to show a fast mode and a slow mode (see Figure 2.9).
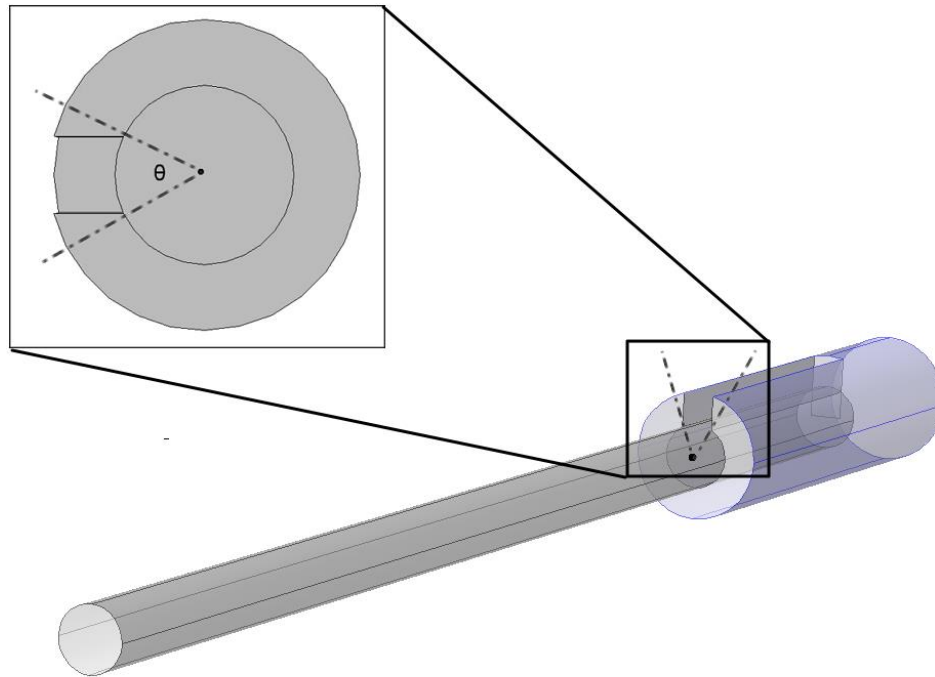


**Figure 2.8** Cylinder tube clamp model designed to demonstrate the effect of defect area on resonance frequency. Constraint conditions are applied to the outer surface of cylinder clamp. The inset illustrates the definition of a size of clamp defect, which is represented by an angle of opening window.
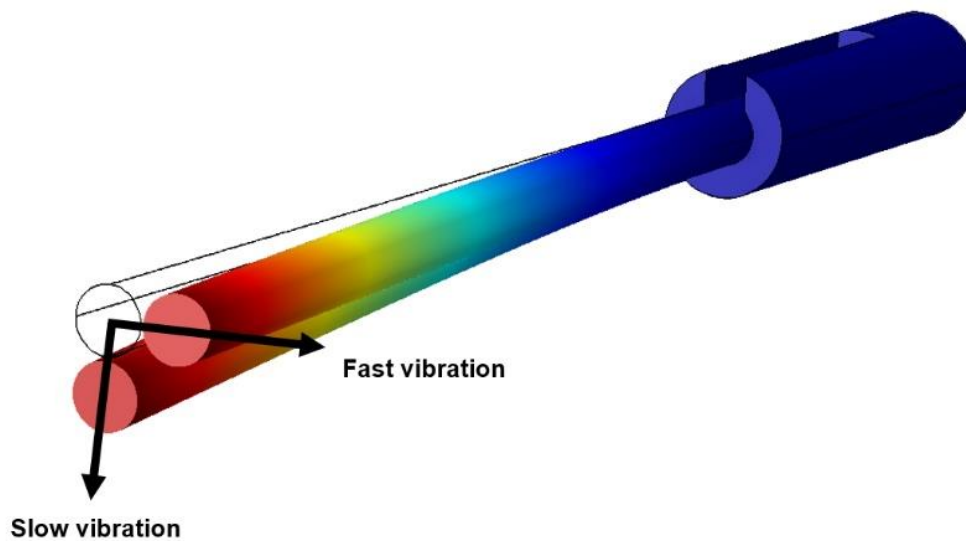


**Figure 2.9** Sketch of two vibration planes with different resonance frequency. The plane of lower frequency vibration will pass through the location of the defect sector.

Simulation vibration frequencies of fast and slow modes are shown in Figure 2.10. The opening angle varies from $5°$ to $175°$ at a step of $5°$ leading to an increasing resonance frequency difference between two modes. The maximum difference of two vibration modes is about 37 kHz when the defect opening angle is $140°$, which is less than 1% of resonance frequency at perfect clamping condition. The meaning of "defect" can be extended to any non-uniform clamping, e.g. Young's modulus of electrodeposited clamp material varies at the clamp-nanowire interface. This asymmetry largely impacts the resonance frequencies of fast and slow vibration mode.
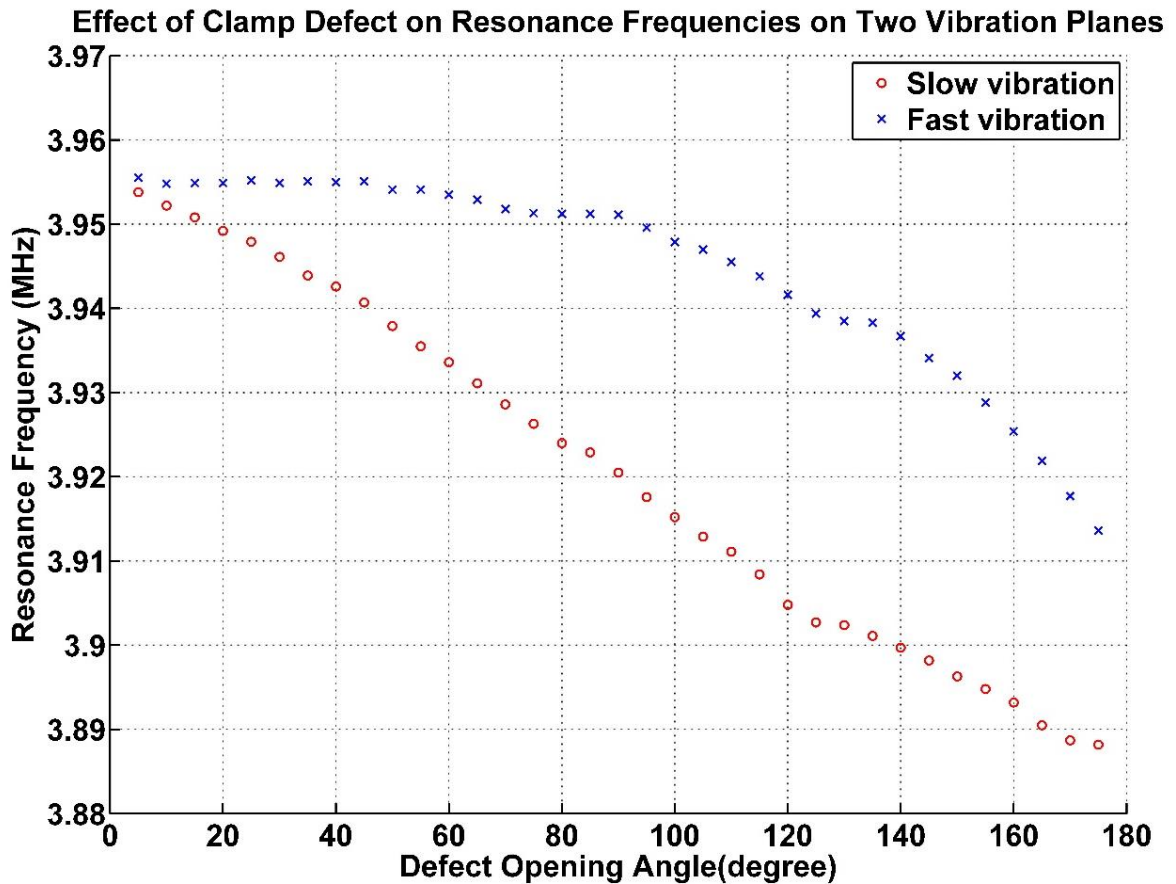


**Figure 2.10** Resonance frequencies of fast and slow vibration modes. For a clamp with no defects, resonance frequency values of the fast vibration and slow vibration modes are identical. With increasing defect magnitude, resonance frequencies of the two vibration states diverge significantly.

## 2.3   Summary and Outlook

Resonance-based measurement is a convenient method to determine nanowire Young's modulus, using the relation from simple beam theory. The accuracy of the method largely depends on the accuracy of resonance frequency and nanowire geometry measurement. In addition, we show, for electrodeposited clamps involved in field-directed assembly the deviations from perfectly rigid and symmetric clamps, which could decrease the accuracy of calculated Young's modulus. A finite element analysis model of cantilevered clamped nanowire resonator allowed simulation of resonance frequency for several clamp conditions.

The simulation indicates that clamped nanowire resonator will generally have smaller resonance frequency compared to the theoretical resonance frequency under rigidly clamped conditions, since clamping part of nanowire is not subjected to the fixed constraint, i.e. the clamp material is compliant.

To ensure the fabricated nanowire resonator has a resonance frequency closer to the theoretical value, we have determined the minimum clamped depth required. When clamped depth is decreased from the minimum required value, the rate of decrease of resonance frequency grows as the clamped depth decreases. When clamped depth is larger than that minimum required clamped depth, the deviation between actual and theoretical resonance frequency remains insensitive to the change of clamped depth.

Compliant clamp material results in nanowire resonance frequency deviating from theoretical values. For clamp materials like rhodium, with large Young's modulus (high stiffness), the nanoresonator shows lower frequency deviation than for relatively soft materials like gold or silver.

Both oblique clamping and defects at clamp interface will introduce asymmetric components in the nanowire resonator system. The resonance frequency splitting to fast and slow vibration modes points to the fact that symmetry is broken, but not severely.

To determine the nanowire Young's modulus without the clamp-induced error in resonance frequency, measuring higher mode frequencies can be helpful [58]. However, both excitation and detection of higher resonance modes are difficult. Zheng et al. have proposed an effective method to filter out clamp uncertainties by measuring fundamental

resonance frequencies with an extra support at different locations along the nanowire [58], [59]. They installed a micromanipulator system inside a scanning electron microscope (SEM) to provide a probe as the extra support. But on a nanowire resonator chip, this manipulation technique is impossible to apply. New ways need to be discovered for filtering out the clamp effect in nanowire resonator mechanical property tests.

# Chapter 3

# Optical Transduction for Measurement of the Resonance Spectrum

Naoelectromechanical systems (NEMS) are promising candidates to replace Microelectromechanical system (MEMS) in a wide range of applications which require miniature dimensions and exceptional sensitivity. Detection of sub-micron displacement, together with high frequency operation requires a transduction method with an extraordinary sensitivity and a large bandwidth, and is still one of the challenging topics in NEMS applications [31]. In this chapter, an optical transduction system is introduced in detail as a scheme to detect resonance frequency spectrum of nanowires. The resonance spectrum of single rhodium nanowire (RhNW) is measured and analyzed for aspects of fundamental resonance frequency ($f_0$) and quality factor (Q).

## 3.1   Optical Transduction Setup

The optical transduction technique was previously developed for measuring the resonance frequency of silicon mesh structures [60]. Successors extended this transduction method and perform ultra-high sensitive measurements of resonance frequency on double-clamped nanobeam [61] and nanowire cantilever [62].

The coherent and narrow probing light beam is provided by a 632.8nm He-Ne laser source (Melles Griot 05-LHP-991). As seen in Figure 3.1, a beam splitter outside the microscope acts to let the probing laser from the source pass through, while reflecting a

portion of the laser power returning from the nanowire resonator chip to a photodetector (New Focus Model 1601FS-AC). The laser light passes through a series of optical elements inside the microscope (Nikon Eclipse Ti-S Inverted Research Microscope, customized) and is finally focused on the tip of the nanowire resonator (see Figure 3.1 and Figure 3.2).
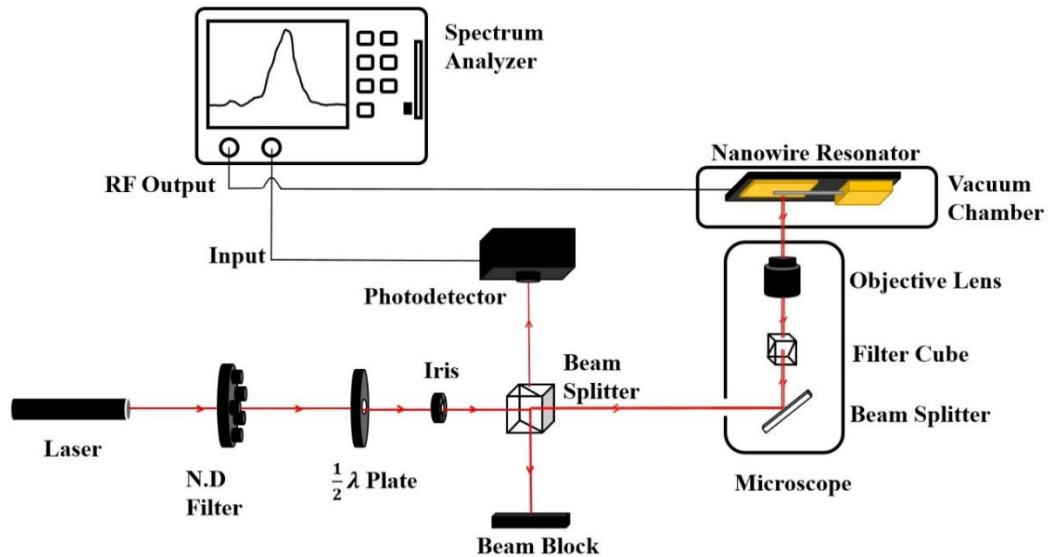


**Figure 3.1** Schematic diagram of optical transduction setup
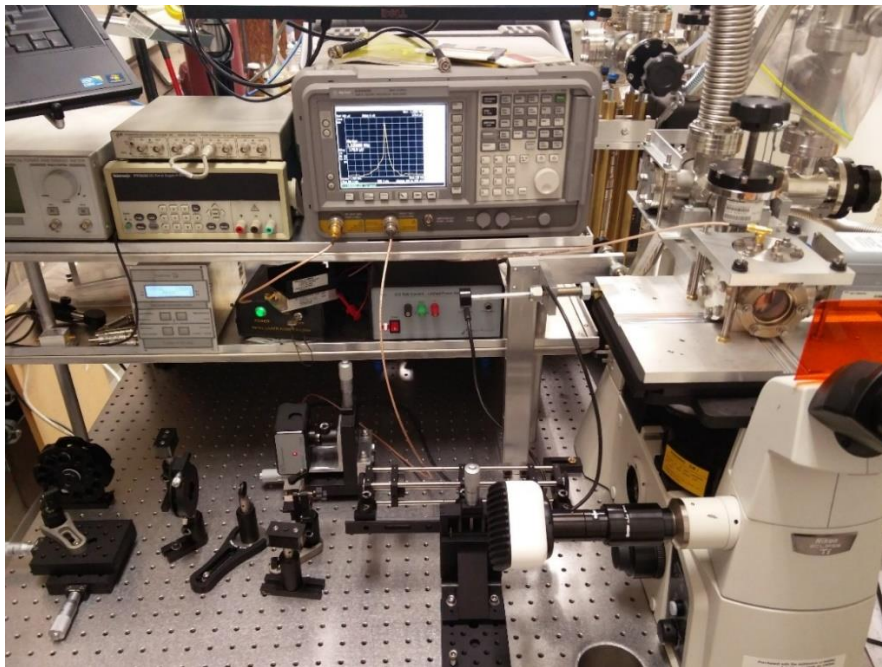


**Figure 3.2** Photo of real optical components and electronic devices used in optical transduction.

The probing light is modulated, carrying information of nanowire resonance, which is reflected back to photodetector. A spectrum analyzer (Agilent E4402B) performs two functions: generating an RF electrical signal to drive piezo actuator underneath the nanowire resonator chip and evaluating the AC signal from the photodetector in the frequency domain. More specifically, the AC driving voltage is amplified right after the RF output of spectrum analyzer. Measuring resonance frequency of nanowire requires an environment with negligible resistance from air molecules. A mechanical pump and a turbo pump work in sequence to maintain the nanowire chip chamber in an ultra-high vacuum condition, typically $10^{-7}$ mbar.
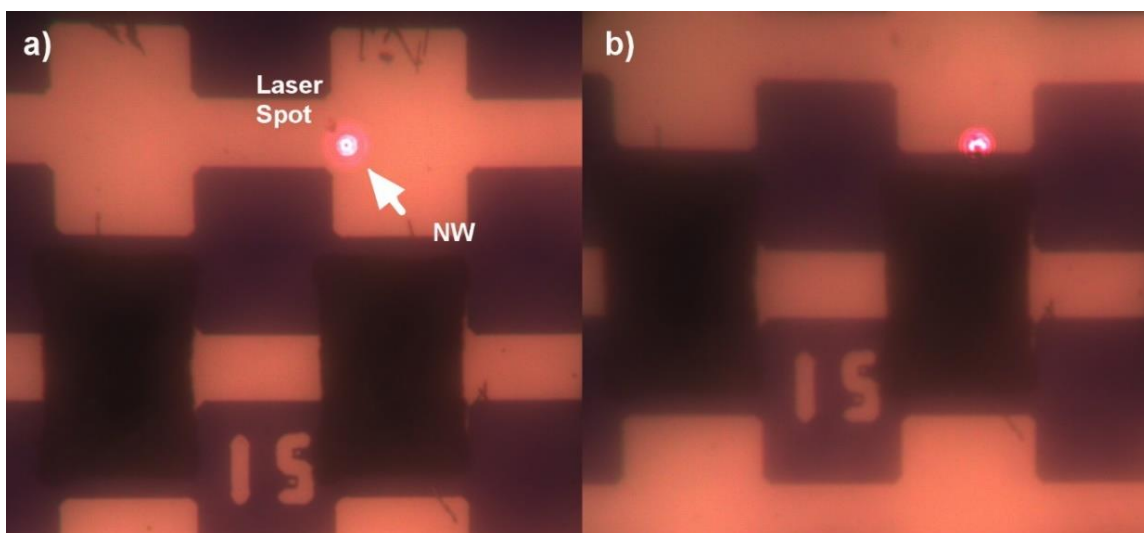


**Figure 3.3** CCD image of positioning nanowire resonator to laser spot centre. a) Nanowire resonator moves towards laser spot. b) Nanowire tip is aligned with center of laser spot.

To conduct the resonance frequency measurement, firstly, laser and spectrum analyzer should be allowed to equilibriate in temperature –we allow warm up time of 20 minutes. Secondly, it is vital to align the laser beam emerging from the objective normal to the chip plane. Upon achieving this alignment, there is no change in shape or movement of the laser spot on the chip, during focusing, which makes it possible to mark the centre of the laser spot on the live CCD camera image. The third step requires positioning the tip of the nanowire resonator on the center of the laser spot by moving the microscope stage that holds the vacuum chamber (see Figure 3.3). Switching on the RF driving voltage and searching for the resonance peak on spectrum analyzer is the final

procedure. For the sake of maximizing the resonance frequency signal, adjusting the plane of polarization, focusing plane and position of photodetector are preferable approaches after the final step.

## 3.2 Rhodium Nanowire Resonator Chip

Rhodium nanowire (RhNW) resonators used in this thesis project were prepared by our group members Nima Moghimian and Mahshid Sam. Dr. Moghimian synthesized the cylindrical RhNWs using electrodeposition within a porous membrane [63]. He chose commercial porous membranes with few hundreds of nanometer pore diameter as templates and evaporated a silver working electrode on one side of the membrane material (see Figure 3.4a). Electrochemical deposition of RhNWs was completed from rhodium sulfate solution inside a customized chamber where platinum is the counter electrode and Ag/AgCl is the reference electrode. Separation of individual RhNWs involved removal of the silver working electrode and membrane material. Rinses of the RhNWs was done first with water and then with ethanol.

Assembly of nanowire resonator was a challenging task finished by Dr. Sam, comprising processes of preparing substrates, positioning nanowires and clamping nanowires [49, 64]. Using photolithography, gold interdigitated electrodes were fabricated on silicon wafers with 300 nm silicon oxide layer. A sacrificial photoresist layer was coated on the substrate to prevent an electrical short circuit during assembly of RhNWs. To position NWs in between electrode pairs, wells were patterned in the photoresist layer using photolithography. Photolithography exposure and developing time was chosen such that the wells had a depth half of the thickness of the photoresist. The NW suspension was then introduced over the substrate while an AC electric field was applied to the interdigitated electrodes. As a result of interaction between dipole moments created in NWs and gradient of the electric field, the dielectrophoresis force generated directs NWs to be positioned inside the wells (see Figure 3.4b). While RhNWs were in their positions, another photoresist layer was coated on the wafer followed by elimination of the photoresist from one of the electrodes from each electrode pairs. Silver was then electrodeposited on these electrodes to clamp one end of the positioned NWs. The

substrate was next soaked in Shipley1165 remover to clean the remaining photoresist. De-ionized water and ethanol were employed to clean the substrate before it was transferred to critical point dryer. The last step was essential to prevent RhNWs from being pulled to the gold electrodes by drying of the solvent.

Biosensing applications of nanowire resonators require functionalization for capturing target biomarker molecules [26]. Separating the processes of nanowire synthesis and field-directed assembly allow functionalization to be done off-chip before assembly. Also, since nanostructures are not patterned individually by expensive techniques such as electron beam lithography, this assembly method enables large-area fabrication at low cost [64]. However, imperfect clamping could bring unwanted influences on nanowire resonance peak spectrum, like multiple peaks, unpredictable influence on polarization effect, etc. This motivated our study of the clamping effect on resonance spectrum.
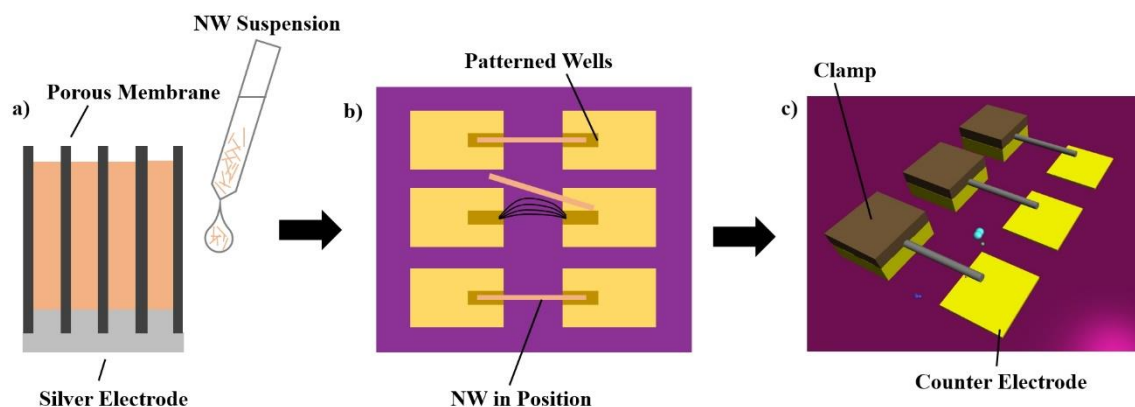


**Figure 3.4** Illustrations of nanowire resonator fabrication process. a) Electrodeposition of RhNWs using nanoporous membrane with silver electrode deposited at the bottom. b) RhNW guided by the dielectrophoresis force to patterned wells. c) 3D illustration of clamped nanowire resonator arrays.

## 3.3  Nanowire Resonator Actuation

Two actuation schemes, piezo disk actuation and electrostatic actuation, are integrated in one framework as shown in Figure 3.5. Nanowire resonator chip is transferred onto a round piezo disk (custom-made based on NEXXTECH Piezo Buzzer, 3.5kHz resonant

frequency) stabilized at each chip edge and point with indium (In) solder material. Three height-controllable copper pillars support the piezo disk, keeping the surface of the chip within 2mm of the vacuum chamber window, facing the objective lens. This mounting connects the brass substrate of piezo disk to the electrical ground outside the vacuum chamber. The spectrum analyzer delivers AC driving voltage through an aluminum contact on the piezoelectric material. Under AC signal, piezoelectric material substrate allows driving vibration over a range of frequencies that vibrates the brass and all nanowire resonators on the chip mounted on it.
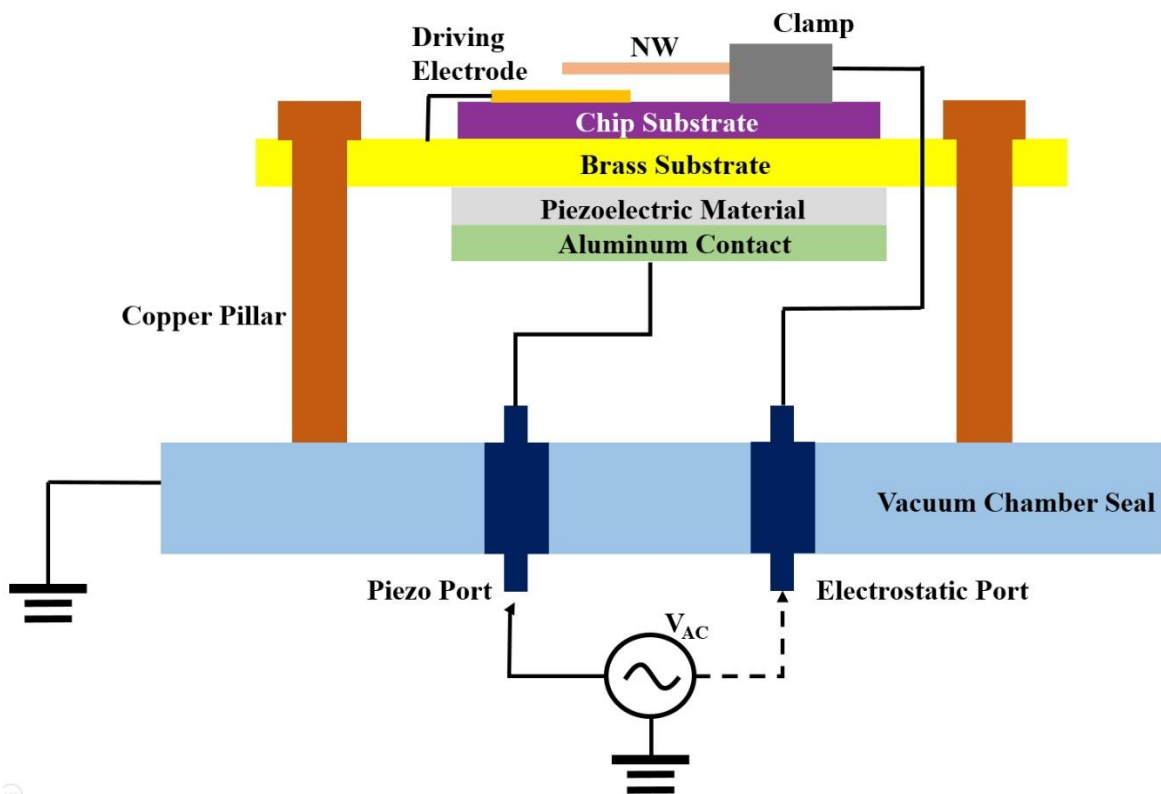


**Figure 3.5** Schematic of piezo disk actuation and electrostatic actuation 2-in-1 framework. AC signal output from the spectrum analyzer can be applied either to the piezo port or the electrostatic port, giving a convenient way to switch between two different actuation methods. The piezo port is connected to the aluminum contact on the piezo disk. Clamp of nanowire resonator is wired to the electrostatic port and the driving electrode is grounded through the brass substrate.

However, the measurement of nanowire resonator could be affected by the characteristics of piezo disk. A non-uniform vibration force could be exerted on nanowire resonator due to the large variation of impedance of piezo disk; this problem is significant while sweeping over a wide range of frequency [65]. The piezo disk is a multi-mode structure, which is sensitive to how it is secured. We have used a frame with three screws, as shown in Figure 3.6. Generally, its excitation is not completely uniform over a frequency range. Soft indium solder may not guarantee a rigid contact between brass substrate and nanowire resonator chip, and this may result in varying energy dissipation for different piezo modes. This loss of energy may require more energy (higher AC driving voltage) and it is difficult to find amplifiers to excite higher frequency resonance. Furthermore, all nanowires with a variety of length on the chip are resonating at the same time when using piezo actuation. Since we have no individual control of the displacement of each nanowire at a certain AC signal, short nanowires with low amplitude of vibration may not give significant response while long nanowires could touch the electrodes in vibration [64] and may be immobilized irreversibly. Considering these situations, piezo disk actuation should be used with special care during measurement of nanowire resonance frequency.

Electrostatic actuation is preferable as it provides a uniform and strong driving force on nanowire resonator. As illustrated in Figure 3.5, AC voltage is simply applied to the clamp and counter electrode beneath the nanowire tip. Induced charges on nanowire generate electric field across nanowire-electrode separations as a result of capacitive coupling [65]. This electrostatic force offers direct energy transduction from electricity to mechanical vibration. Another advantage of electrostatic actuation is, with the help of lead wire bonding, individually patterned nanowire resonators can be directly wired to the AC signal, making single nanowire resonator operation at a time possible. But for the pattern in which all nanowire clamps are electrically connected and all counter electrodes are electrically connected, electrostatic actuation is possible only if no short circuit has occurred over the entire chip, that is, no RhNW touches the counter electrode. This is a challenge for the current assembly process. This is the reason why electrostatic drive was not used in the setup of Figure 3.6. Single nanowire devices have, in the past, been isolated and addressed by wire bonding to their contacts.
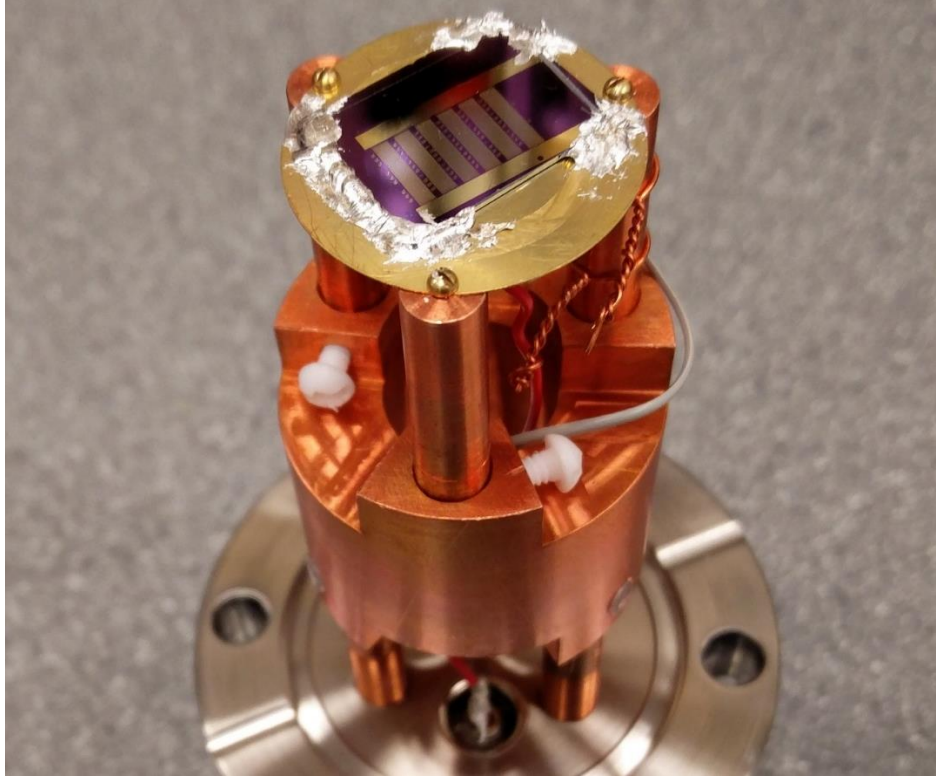
**Figure 3.6** Photo of nanowire resonator actuation assembly mounted on the vacuum chamber flange. Piezo disk actuation is used in this setting. Since short circuit would occur on this type of chip, electrostatic actuation was not used for this chip.

## 3.4   Resonance Frequency of Rhodium Nanowire

Two characteristics of the nanowire resonator frequency spectrum are commonly of interest, the resonance peak frequency $f_0$ and quality factor (Q-factor). In Chapter 2, the equation to calculate the resonance frequency has been presented. Q-factor is an indicator of energy loss in a resonant system not limited to mechanical system. For Q >> 1, the approximation of Q is written as

$$Q \approx \frac{f_0}{\Delta f_{1/2}} \tag{3.1}$$

where $f_0$ is the center frequency of resonance peak, $\Delta f_{1/2}$ is the full width at half-power maximum of resonance peak. If the resonator vibrates in a high damping environment, resonance peak spectrum will get broader ($\Delta f_{1/2}$ becomes larger) resulting in a lower Q

value. Figure 3.7 illustrates how the Q-factor can be estimated from the resonance spectrum.
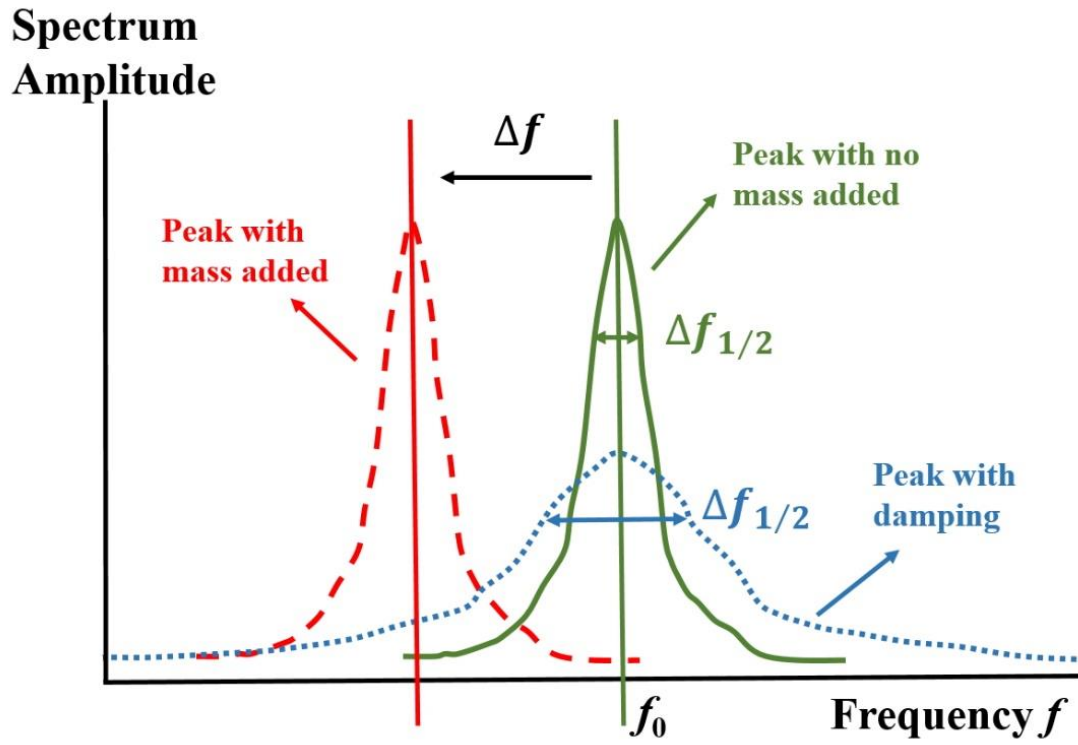


**Figure 3.7** Schematic of the spectrum of nanowire resonator. Green solid peak is the natural resonance frequency spectrum. If additional mass is attached to the nanowire, the spectral peak of resonance will shift to a lower frequency as shown by the red dashed curve. Blue dot spectrum shows a low Q-factor spectrum, obtained, for example, if the nanowire resonator is operated in a high fluid damping environment.

The sensitivity to added mass may be calculated from

$$\frac{\Delta f}{f} = -\frac{1}{2}\frac{\Delta m}{m} \tag{3.2}$$

where $m$ and $f$ are the mass of nanowire and resonance frequency before added mass, $\Delta f$ is the frequency shift after added mass and $\Delta m$ is added mass.

Characterization of the RhNWs (A-01, A-21, C-75) are performed at high vacuum, with absolute pressure of $1.2 \times 10^{-7} mbar$ at room temperature. Roughly 4mW laser power is focused on the free tip of nanowire, with a 20mV driving voltage output from the spectrum analyzer. Figure 3.8 displays the fundamental resonance frequency peak

(100 averages) of RhNW A-21. It is straightforward to determine the peak center is 1.334MHz and calculate the quality factor of ~400 using Equation 3.1. From the SEM picture (see Figure 3.9), the geometry of this nanowire is determined, having a diameter of 420nm and length of 13μm. Taking rhodium density to be 12,450kg/m$^3$ and Young's modulus of bulk polycrystalline rhodium to be 379GPa [66], the theoretical fundamental resonance frequency (using $\beta_0$=1.875) is 1.921MHz calculated by Equation 2.1. From COMSOL model results in Figure 2.5, we know that for a comparable RhNW (length of 10μm and a diameter of 400nm), gold or silver clamp may result in -3.3% of frequency deviation from theoretical value. Applying -3.3% correction to theoretical frequency, we expect that measured frequency should be 1.858MHz which is still far away from 1.334MHz. Clamped depth is another factor that can make resonance frequency lower than the theoretical value but it is impossible to measure with SEM images. Without considering clamp compliance or depth, this discrepancy could at first suggest that Young's modulus of fabricated RhNW is significantly lower than the bulk value in the handbook. Calculation of measuring Young's modulus of RhNW based on detected resonance frequency gives a value of 183GPa. In another study of comparable rhodium NWs, the Young's modulus measured in the work of Li et al. is (222$\pm$70 GPa) [67]. Measurement results of all three RhNWs are listed in Table 3-1. Resonance frequencies of RhNWs A-01 and C-75 in the table are the highest resonance peaks in the spectrum for each nanowire. Young's modulus of those two nanowires are hard to determine since multiple resonance peaks exist in the spectrum. The two Young's modulus values shown in Table 3-1 were calculated from the dominant peak frequency of each nanowire.

**Table 3-1** Summary of RhNW Resonance Frequency Measurement and Calculated Young's Modulus

| Nanowire | Length (μm) | Diameter (nm) | $f$ (MHz) | E (GPa) | Q factor |
|----------|-------------|---------------|-----------|---------|----------|
| A-01 | 10.0 | 450 | 2.966 | 276 | 724 |
| A-21 | 13.0 | 420 | 1.334 | 183 | 400 |
| C-75 | 9.2 | 450 | 2.915 | 191 | 225 |
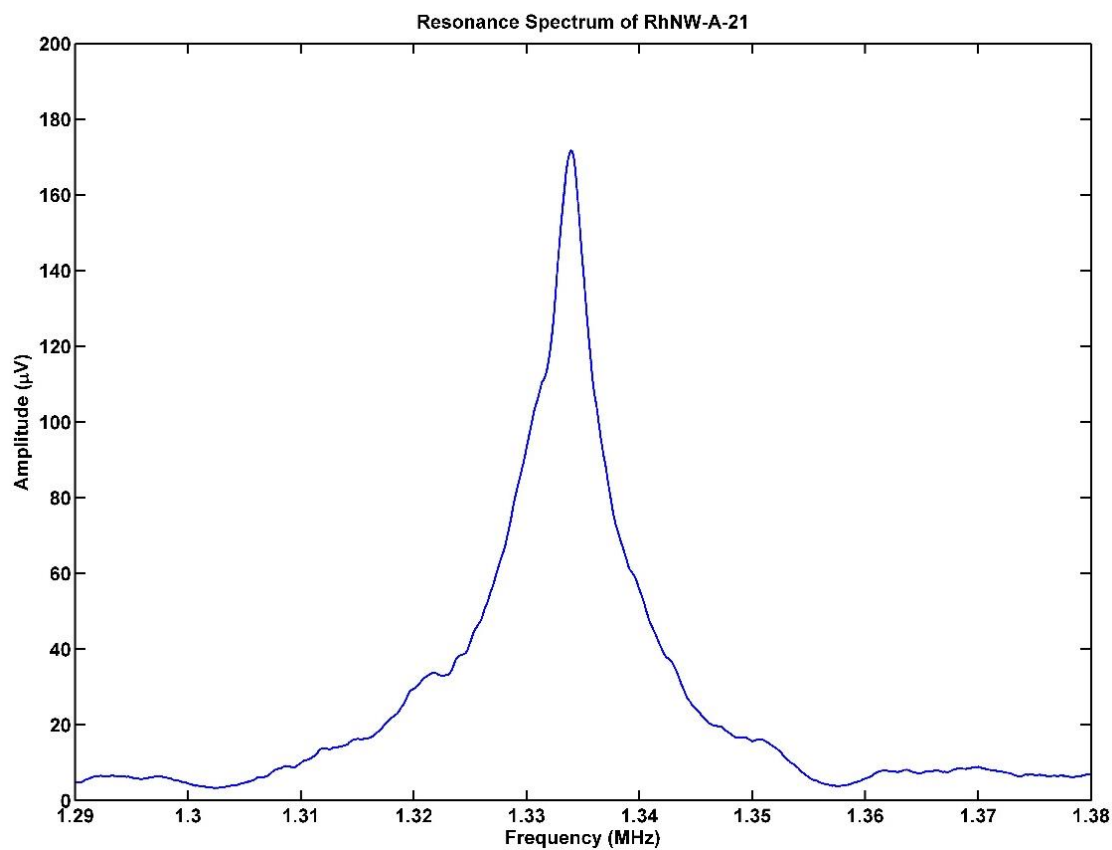
**Figure 3.8** Resonance frequency peak of RhNW A-21



1.0kV 8.3mm x6.00k SE(M) 8/28/2014          5.00um
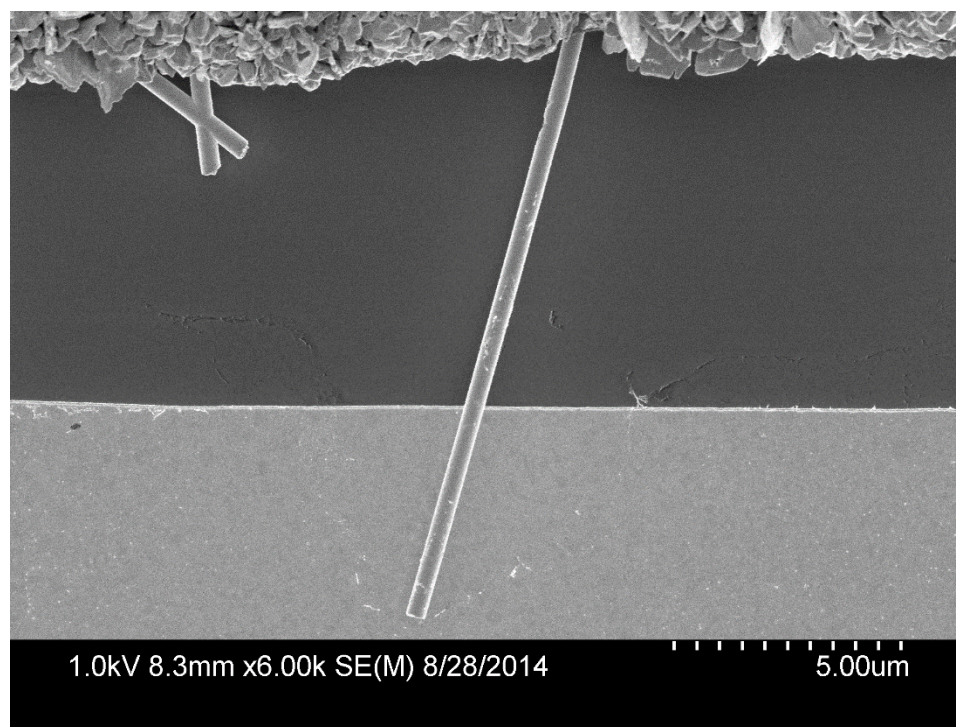
**Figure 3.9** Top-view of the RhNW A-21 SEM image after FIB process.

## 3.5    Summary and Outlook

The optical transduction method is described in this chapter with complete introduction of each component and measurement procedure. RhNWs were prepared using electrodeposition and nanowire resonators assembled using dielectrophoretic force. Piezo disk and electrostatic actuation are integrated in one framework for easy switching between these two actuation systems. Resonance frequency measurement of RhNW resonator offers a way to characterize Young's modulus of rhodium nanowire.

# Chapter 4

# Light-Nanowire Interaction: Effect of Laser Power and Polarization

Optical transduction setup has been described in Chapter 3 as a method of detecting the resonance frequency spectrum of nanowire mechanical resonators. Resonance peak center frequency and peak amplitude are the two main characteristics we are concerned with in this study of the resonance frequency spectrum. Resonance peak center frequency shift with added mass is the basis for sensitive mass detection [30]. Early-stage diagnosis of cancer has been demonstrated by the detection of resonance frequency shift induced by RNA biomarker bound to functionalized nanowires [26]. Accurate measurement of added mass requires the resonance frequency shift to depend solely on the added mass. However, strong heating from the probing laser could also introduce softening effect of the resonator and therefore affect the resonance frequency [68]. It is worthwhile to examine the relationship between input laser power and resultant resonance frequency of the nanowire resonator as well. Understanding the magnitude of the effect of laser power will help to differentiate the cause of resonance frequency shift in mass sensing. Moreover, under some unfavorable conditions, the high noise level may become comparable to or greater than the resonance peak amplitude making it hard or impossible to determine the resonance frequency. Higher amplitude of resonance peak (signal-to-noise ratio, SNR) would definitely aid in resonance frequency spectrum determination. This resonance spectrum is transduced by the interaction between nanowire and laser beam – laser power scattered back by the nanowire is modulated at its

vibration frequency. A simple way to improve the SNR is to increase the laser power. However, as mentioned above, the resonance frequency shift resulting from the choice of laser power setting could itself affect the frequency, causing errors in application such as mass detection. Is there any other factor that can affect the amplitude of the resonance peak signal? Researchers have observed significant enhancement of scattered intensity from silicon nanowire when the laser is polarized parallel to the nanowire axis [69]. Hence, understanding polarization-dependent scattering is required for correct measurement, interpretation and accurate use of the resonance spectrum.

## 4.1   Light-Nanowire Interaction Optical Setup

To investigate light-nanowire interaction, the plane of laser polarization and selected laser power setting are two input variables of particular interest to this work. The experimental setup is based on optical transduction, introduced in Section 3.1. Neutral density (N.D.) filters are deployed to change laser power by simply rotating the specific N.D. filters into the optical path. The N.D. filter device comprises of two rotating disk mounts, each with multiple optical plates of different N.D. ratings (0.1 to 5.0). Recording the resonance frequency spectrum following the optical transduction method with different input power selected by N.D. filters thus gives the dependency of nanowire resonance peak on input probing laser power.

First, we make the plane of laser polarization (electric field vector) to be perpendicular to the optical table surface before introducing half-wavelength plate. To do so, we use a polarizing beam splitter (PBS) cube and power meter and rotate the laser tube until minimum power is obtained (see Figure 4.1a). We then introduce the half-wave plate upstream of the PBS cube and rotate it until the same minimum power reading is obtained (see Figure 4.1b). We set the scale that marks the rotation angle of the half-wave plate to zero. At this position, the fast axis of half-wavelength plate is aligned parallel to zero setting, the plane of laser polarization staying perpendicular to table surface as long as half-wavelength plate does not rotate (staying at $0°$ on scale). When the half-wavelength plate is rotated by an angle $\delta$, the plane of polarization rotates by $2\delta$. This means that if the polarization scale reading is $0°$, $90°$, $180°$ or $270°$, the plane of

polarization is perpendicular to the table surface; and if set to 45 °, 135 °, 225 ° or 315 °, it is parallel to the table surface.
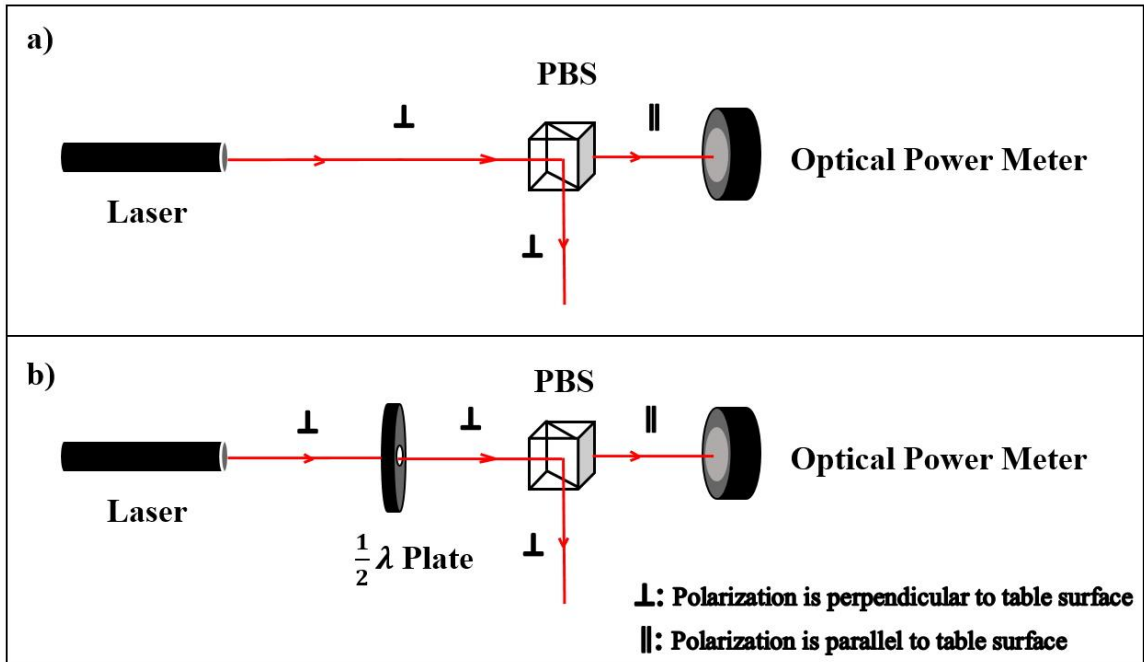


**Figure 4.1** a) Alignment of the polarization coming out of laser tube perpendicular to the table surface. Polarizing beamsplitter (PBS) cube only allows the polarization component parallel to the table surface to be transmitted. Therefore, by rotating the laser tube, when polarization is perpendicular to the table surface, minimum power value would be read on power meter. b) Alignment of half-wave plate with its scale. Half-wave plate is rotated until minimum power reading is obtained. Then we set the scale that marks the rotation angle of the half-wave plate to zero.

The starting orientation angle $\theta_0$ between nanowire axis and perpendicular (to table surface) polarization state is determined by a thin copper wire mounted vertically (to table surface) at iris (see Figure 4.2). The copper wire blocks a portion of the laser beam and casts a shadow on the nanowire resonator chip, which can be captured by CCD camera with nanowire resonator together (see Figure 4.3). If the half-wavelength plate rotates counter-clock wise, the angle $\theta$ between plane of laser polarization and nanowire axis is calculated as

$$\theta = \theta_0 - 2\delta \tag{4.1}$$

where θ is in the range 0° to 360°. Variable orientation angle θ generated by rotating half-wavelength plate and the corresponding resonance frequency spectrum are then analyzed to unveil the interaction between laser polarization and nanowire resonator.
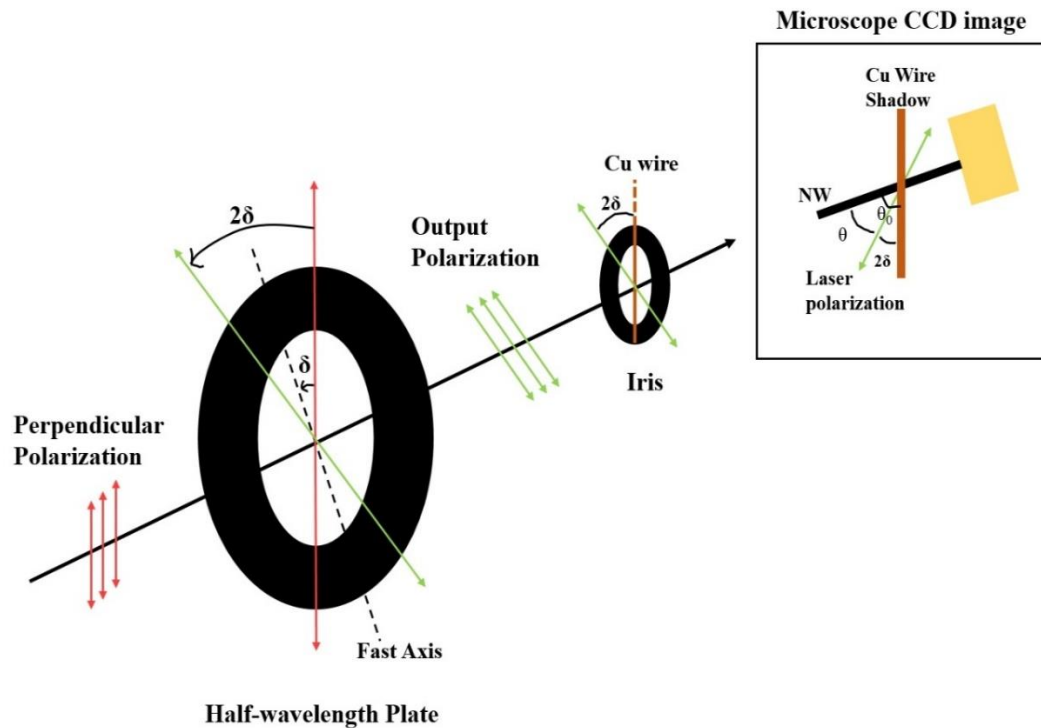


**Figure 4.2** Sketch of optical components alignment for laser polarization effect experiment.
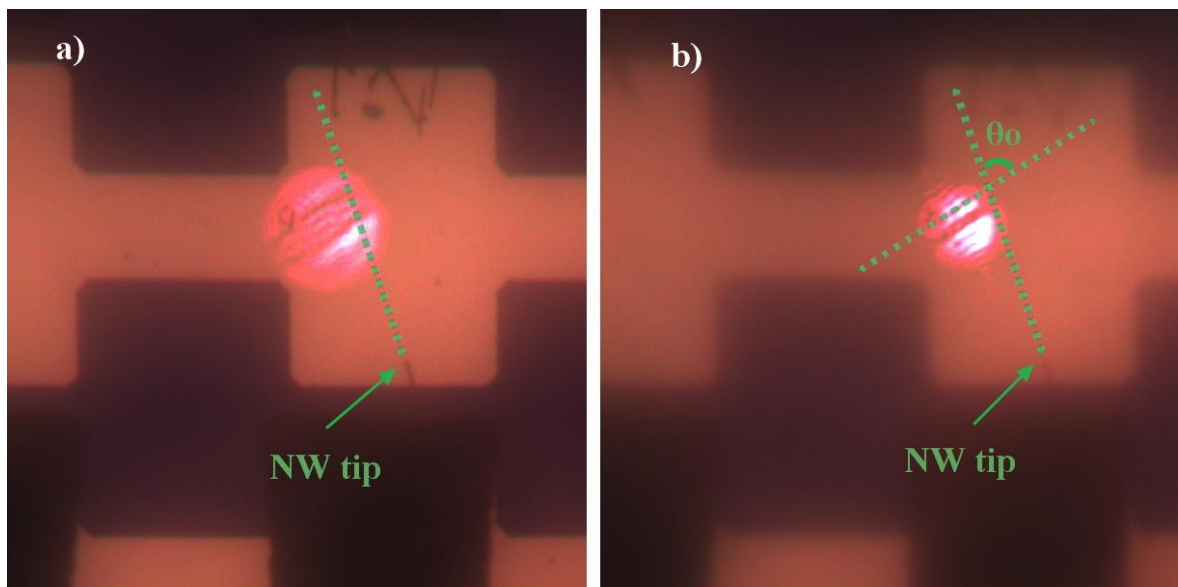


**Figure 4.3** CCD images of determining initial orientation angle between nanowire and copper wire shadow. a) Microscope imaging plane is focused on the nanowire and the

orientation of its axis is determined along the green dotted line extended from nanowire tip. b) Objective lens is moved until the shadow of copper wire appears in the laser spot. Another green dotted line represents the orientation of wire. Initial orientation angle $\theta_0$ is the acute angle between two green dotted lines.

## 4.2 Earlier Study of Laser-Silicon Nanowire Interaction

University of Victoria Engineering undergraduate student Serge Vincent was the first to find the strong influence of the plane of the laser polarization on nanowire resonance spectrum peak amplitude and frequency, for a single-crystal silicon nanowire (SiNW) using the orientation angle determination method describe in Section 4.1.
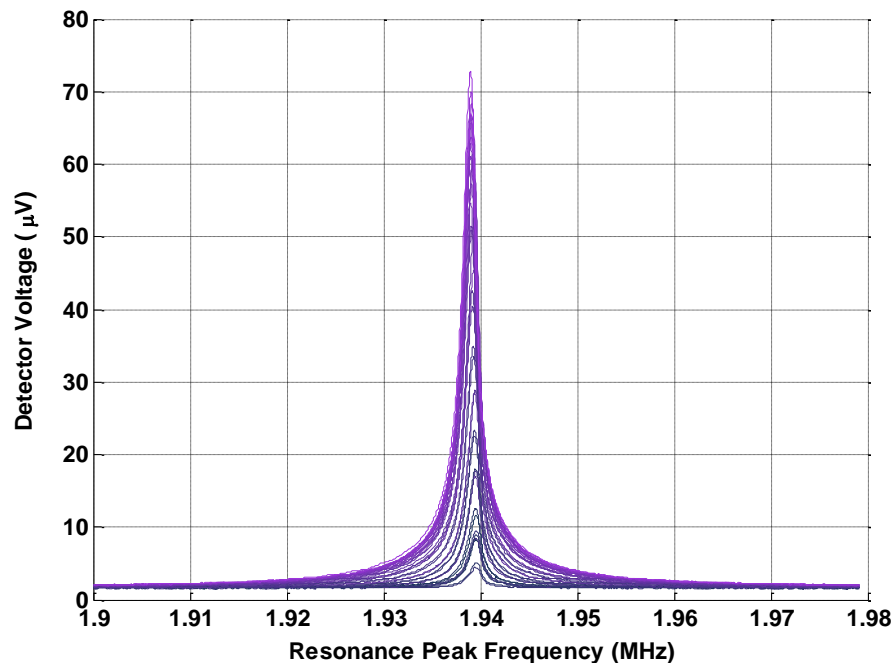


**Figure 4.4** Collection of spectra at different laser polarization states. The amplitude of the spectra show a significant variation from 5µV to 73µV at the same laser power. The weakest signal was recorded when the laser polarization was perpendicular to the nanowire axis while the strongest one was achieved with laser polarization parallel to nanowire axis. A small frequency shift can be observed when comparing the peak center frequency of weakest and strongest spectra.

The SiNW dimensions, as measured by scanning electron microscopy (SEM), were 11.8μm length, and a diameter of 330nm. Initial orientation angle $\theta_0$ was measured as 26°. Resonance frequency spectra under multiple polarization states were measured at a chamber pressure of $3 \times 10^{-11}$ atm and plotted in Figure 4.4. The amplitude of the resonance frequency peak varied significantly over a 360° range of orientation angle, with a minimum signal amplitude of 5μV and a maximum of 73μV. Besides, the lowest amplitude signal possessed the highest resonance frequency. The center frequency of resonance peak was reported to shift slightly to lower values with increase of signal amplitude.

**Normalized Spectral Peak Amplitude**
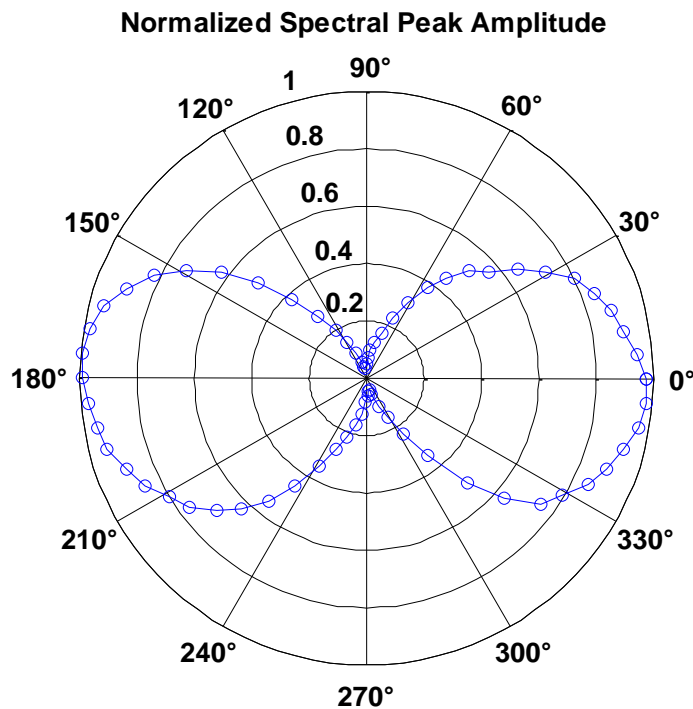


**Figure 4.5** Polar plot of normalized spectral peak amplitude in an orientation angle of 360 degree. The maximum peak amplitude is attained at orientation angle of 0° and 180° in which the laser polarization is parallel to the SiNW axis. A considerable loss of 96% of signal amplitude is detected as polarization state is set perpendicular to SiNW axis (90° and 270° in the figure).

It is easier to visualize the result using polar plots to show the signal amplitude variance and resonance frequency shift with orientation angle. In polar plots, 0° and 180° represent laser polarization parallel to the nanowire axis, while 90° and 270° denote the

perpendicular state. Any angle other than these four orientation angles is the polarization state between parallel and perpendicular states. Resonance peak amplitudes normalized by the maximum value measured (73µV), are plotted in Figure 4.5. 96% signal amplitude reduction is seen at perpendicular polarization state compared to parallel one. Further the orientation for the most unfavorable signal amplitude corresponds to an upshift of resonance frequency of 0.63kHz which is shown in Figure 4.6.

**Resonance Peak Frequency Shift (kHz)**
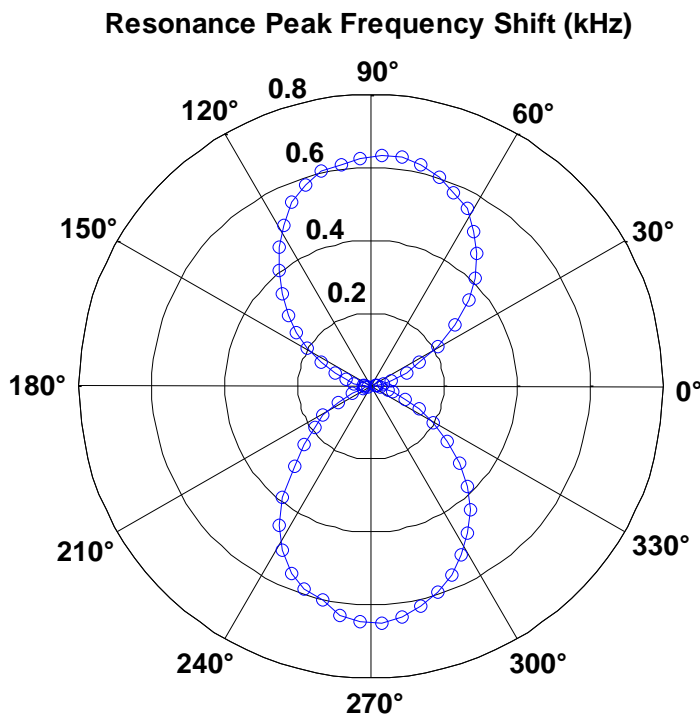


**Figure 4.6** Polar plot of resonance frequency shift with an orientation angle variation of 360°. The resonance frequency measured with polarization state parallel to SiNW axis shows the minimum value. Electric field perpendicular to SiNW axis increases the detected resonance frequency about 0.63kHz.

# 4.3 Laser Heating Effect on Rhodium Nanowire Resonators

Serge Vincent's study focused on silicon nanowires. How does behavior of fine-grained metallic wire differ? We investigated the behavior of suspended rhodium nanowires

(RhNW), synthesized by electrodeposition [63] and clamped using field-directed assembly [64].

Resonance frequency of RhNW A-21 (L = 13μm, D = 420nm) and RhNW E-76 (L = 10.8μm, D = 445nm) were measured under a pressure of $1.2 \times 10^{-7}$ mbar at room temperature. SEM images of these two nanowires are shown in Figure 4.7. The spectrum analyzer provided a 20mV driving voltage, which was amplified by a Mini Circuits amplifier, and used for vibrating the nanowire chip. One hundred spectra were averaged to record the resonance spectrum. The filter cube was taken out of the microscope to maximize the laser power reaching the nanowire resonator. N.D. filters with optical densities from 0.1 to 1.0 were utilized to vary the input laser power. Laser polarization was set parallel to the nanowire axis. The maximum input laser power was 4mW. Figure 4.8a illustrates the resonance peak amplitude detected upon different input laser power. Increasing input laser power results in a linear increase of the resonance peak amplitude.
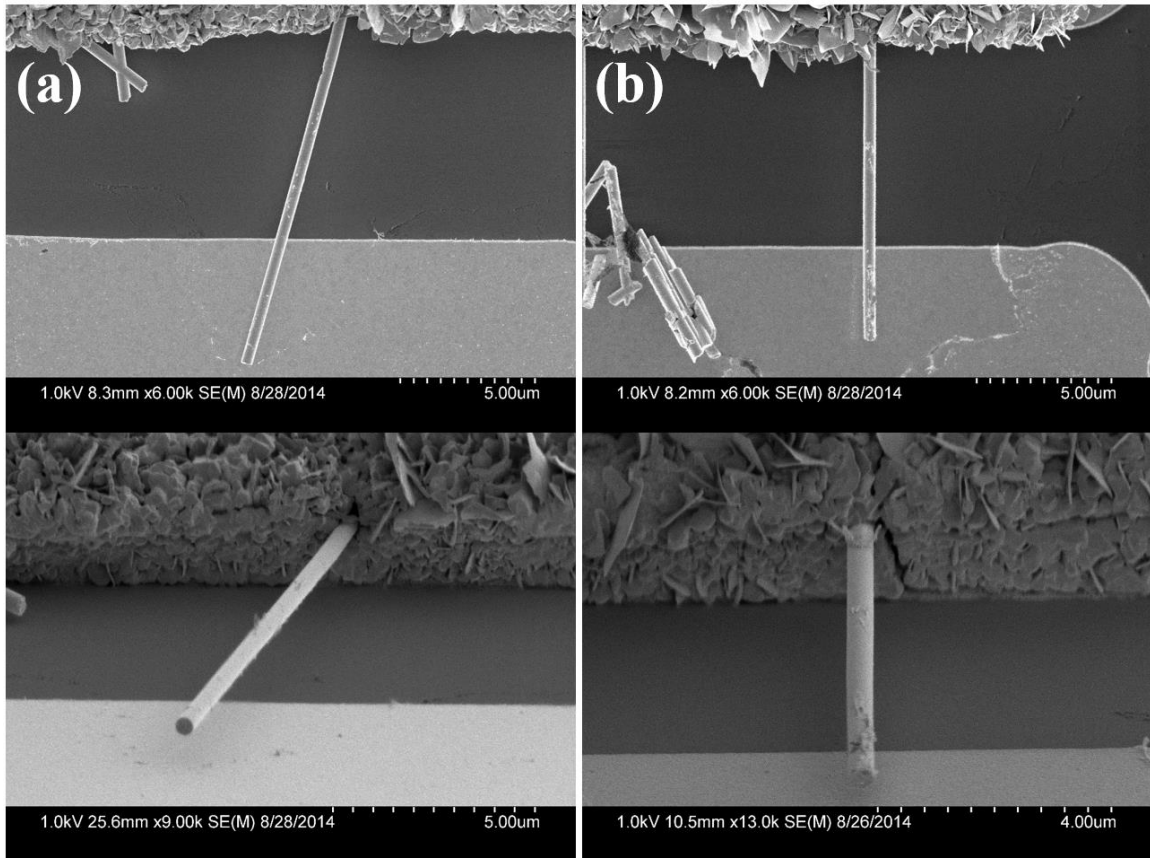


**Figure 4.7** SEM images of nanowire's top-view and side-view: a) RhNW A-21; b) RhNW E-76. Both of the nanowires have smooth surface and good clamping condition.
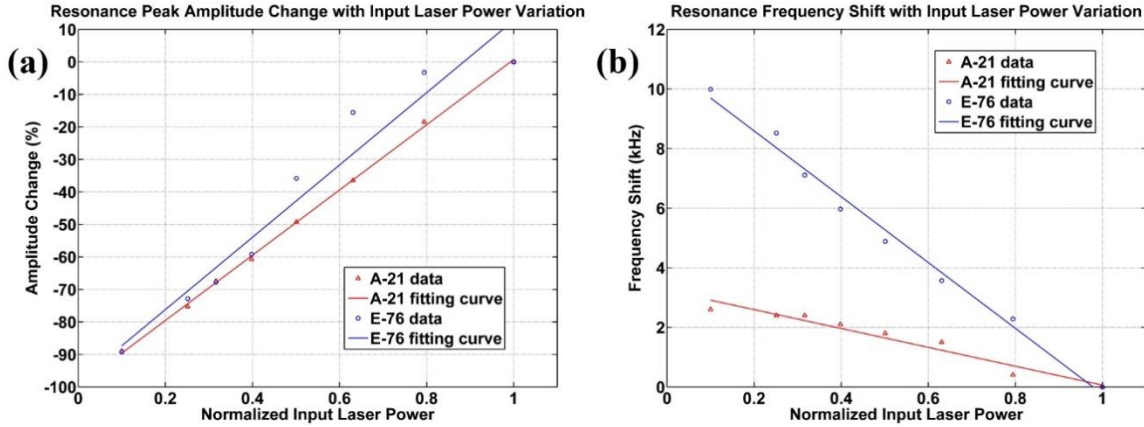
**Figure 4.8** a) Plot of resonance peak amplitude response to different input laser power. The resonance peak amplitudes show an excellent linear relationship with the increasing of input laser power. b) Plot of resonance frequency shift with increase of input laser power. As input laser power grows, the resonance frequency linearly downshifts.

As shown in Figure 4.8b, resonance frequency also shows a linear variation with input laser power, decreasing as higher input laser power is used. The relationship between laser power and resonance frequency could be explained by laser heating effect on the nanowire. The laser beam is not only scattered by the nanowire but also couples energy to the nanowire. The resultant heated state could be changing the mechanical property of nanowire, mainly the Young's modulus, leading to the resonance frequency shift.

In Equation 2.1, no parameter reflects the influence of temperature but we can define a material property parameter $M$ as

$$M = \frac{E}{\rho} \tag{4.2}$$

Therefore, resonance frequency equation can be written as

$$f = \frac{\beta^2}{8\pi} \frac{D}{L^2} \sqrt{M} \tag{4.3}$$

Derivative of resonance frequency $f$ is

$$\Delta f \approx \frac{\partial f}{\partial M} \cdot \Delta M = \frac{\beta^2 D}{16\pi L^2} \sqrt{M} \cdot \frac{\Delta M}{M} \tag{4.4}$$

Resonance frequency $f_0$ under power $P_0$ is 1.3309 MHz, and

$$f_0 = \frac{\beta^2}{8\pi} \frac{D_0}{L_0^2} \sqrt{M_0} \qquad (4.5)$$

We can have

$$\Delta f \approx \frac{f_0}{2} \cdot \frac{\Delta M}{M_0} \qquad (4.6)$$

Figure 4.8 indicates a linear relationship between frequency shift and power rating difference, which gives

$$\Delta f = a_1 \cdot \frac{\Delta P}{P_0} + a_2 \qquad (4.7)$$

where constants $a_1$, $a_2$ are with the same dimension of $f$. Take RhNW A-21 as an example, $a_1$ and $a_2$ can be obtained from plot in Figure 4.8b, $a_1$ = -3.17 (kHz), $a_2$ = 3.23 (kHz). Substitute $\Delta f$ in Equation 4.7 with Equation 4.6, relationship between material property and power rating difference is shown as

$$\frac{\Delta M}{M_0} = \frac{2}{f_0}(a_1 \cdot \frac{\Delta P}{P_0} + a_2) \qquad (4.8)$$

Since density of nanowire remains unaltered ( $\rho \approx const.$ ),

$$\frac{\Delta M}{M_0} = \frac{\Delta E}{E_0} \qquad (4.9)$$

can be derived from Equation 4.2. Finally Young's modulus difference depending on power rating difference demonstrates a linear relationship,

$$\frac{\Delta E}{E_0} = \frac{2}{f_0} \cdot (-3.17 \cdot \frac{\Delta P}{P_0} + 3.23) \qquad (4.10)$$

Equation 4.10 shows the resonance frequency shift upon input laser power variation results from the temperature-dependent Young's modulus. With the increasing of laser power, Young's modulus decreases accordingly leading to the resonance frequency downshifting. In our experimental result, when using maximum input laser power, Young's modulus of RhNW A-21 decreases about 1% corresponding to ~40 ℃ temperature rise [70].

Laser heating effect has been reported on ultrathin nanocantilevers in which resonance frequencies can be reduced with the effect of surface stress generated by laser

power absorption [71]. The resonance frequency shift is presented as a result of a change in the temperature-dependent Young's modulus induced by laser power [68]. Gil-Santos et al. explained the resonance frequency shift for SiNWs as a combination effect of bolometric effect and radiation pressure [72]. For thicker nanowires, the bolometric effect (temperature-dependent Young's modulus) dominates, i.e. resonance frequency becomes lower with the increase of input laser power. Also, the bolometric effect could introduce thermoelastic damping to the resonator [73]. Our experimental evidence shows RhNW has similar resonance frequency shift phenomenon which could be governed by the bolometric effect as well. According to the study of the rhodium Young's modulus of rhodium and its variation with temperature [70], Young's modulus decreases about 5% when temperature rises from 0 ℃ to 200 ℃; this would decrease resonance frequency by 2.5%. This magnitude of frequency change is large enough to result in gross inaccuracies in mass detection applications.

## 4.4    Microscope Effects on Probing Laser

The strong dependency of resonance peak amplitude and resonance frequency shift on plane of laser polarization found for SiNW is fascinating and a deeper understanding of optical transduction would be helpful to discover more facts. The microscope (Nikon Eclipse Ti-S) was regarded as neutral to input laser polarization, that is, it was assumed to keep the laser output polarization exactly the same as input. However, the filter cube and beam splitter installed inside the microscope are shown to have non-negligible influence on the output, depending on different polarization states of the input laser, as described below.

The beam splitter mounted within the bottom of the microscope body directs the laser beam from the side port up to the objective lens. The filter cube installed between the microscope beam splitter and objective lens reflects the white light to illuminate the sample on the observation platform. The beam splitter cannot be dismounted, while the filter cube is removable.

The transmittance of the microscope with single beam splitter (BS only) or with both filter cube and beam splitter (FC & BS) are evaluated in two path setups: single-trip and

round-trip. In single-trip path setup, laser beam only transmits through microscope once and the output laser power is recorded at position 2 on observation platform. Round-trip path features laser's twice crossings through microscope fulfilled by a gold mirror reflecting laser back at position 2. The output laser power $P_{out}$ is collected at position 3 using an optical power meter. The input laser power $P_{in}$ is always measured at position 1 in the Figure 4.9 for both paths. The transmittance $T$ is defined as:

$$T = \frac{P_{out}}{P_{in}} \tag{4.11}$$
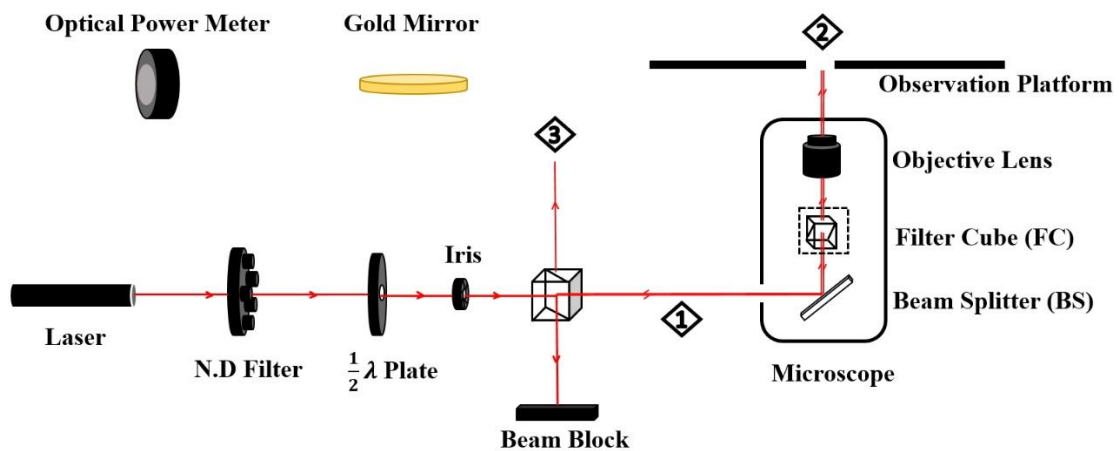


**Figure 4.9** Schematic of single-trip and round-trip paths setup for evaluating filter cube and beamsplitter dependencies on input laser polarization. Position 1 is where input laser power measured. For a single-trip path, the laser beam only crosses the microscope once and output laser power is measured at position 2, using the optical power meter. For the round-trip path setup, a gold mirror is fixed at position 2, reflecting the laser back to the microscope and the output laser power is measured at position 3.

Figure 4.10 shows the transmittance of microscope in a single-trip test. With beam splitter only, inside the microscope, the transmittance remains nearly unchanged even when the laser polarization changes over a 360 °range. But once the filter cube is installed, the transmittance displays a clear polarization-dependent phenomenon. When the plane of laser polarization is parallel to the table surface (90 °and 270 ), the transmittance reaches its highest value, 41%. However, when it is perpendicular to the table surface, it shows a transmittance of only 25%. The filer cube, therefore, has a strong polarization

dependency that can vary the laser power on nanowire resonator when the polarization changes.
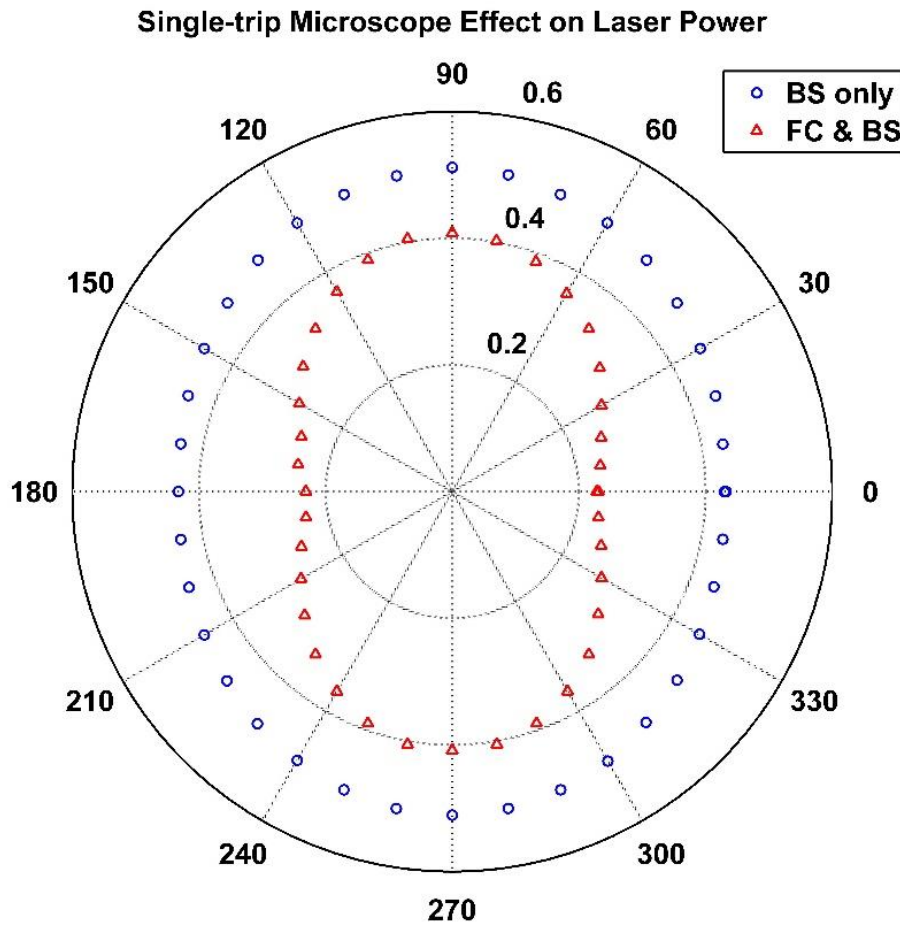


**Figure 4.10** Microscope output laser power dependence on a full 360 ° range of laser polarization angles in a single-trip path. With only the beam splitter (BS only) used, laser output power varies in a small range from 45% to 50% of the input power at different input laser polarization angles. Installation of both filter cube and beam splitter (FC & BS) leads to a 15% output power variation between perpendicular and parallel (to table surface) input laser polarization states.

Transmittance of the microscope shows a stronger dependence on input laser polarization in the round-trip setup (see Figure 4.11) due to two laser passes through optical components inside the microscope. For example, with use of the BS cube only, the maximum value of $T$ is 0.5 in the single-trip setup. In the round-trip setup, another half of the laser power is lost due to the beam splitter inside of the microscope after it is

reflected back by the gold mirror. A further 50% reduction of laser power takes place when the reflected laser hits the beam splitter outside, before being collected by photodetector. Thus, the maximum $T$ is 0.125 ($0.5×0.5×0.5$) in round-trip setup. When the filter cube is removed (only BS remaining), the shape of the transmittance polar plot contracts at $0\,°$ and $180\,°$ position, from a circle to a racetrack-like shape, indicating the perpendicular input polarization results in a relative weaker output laser power. If both filter cube and beamsplitter (FC & BS) are installed, the output laser power at which the laser polarization is perpendicular to table surface is only 1/3 of which the polarization is parallel. There is a considerable loss of output power with plane of laser polarization perpendicular to table as seen from the peanut-shaped transmittance polar plot.
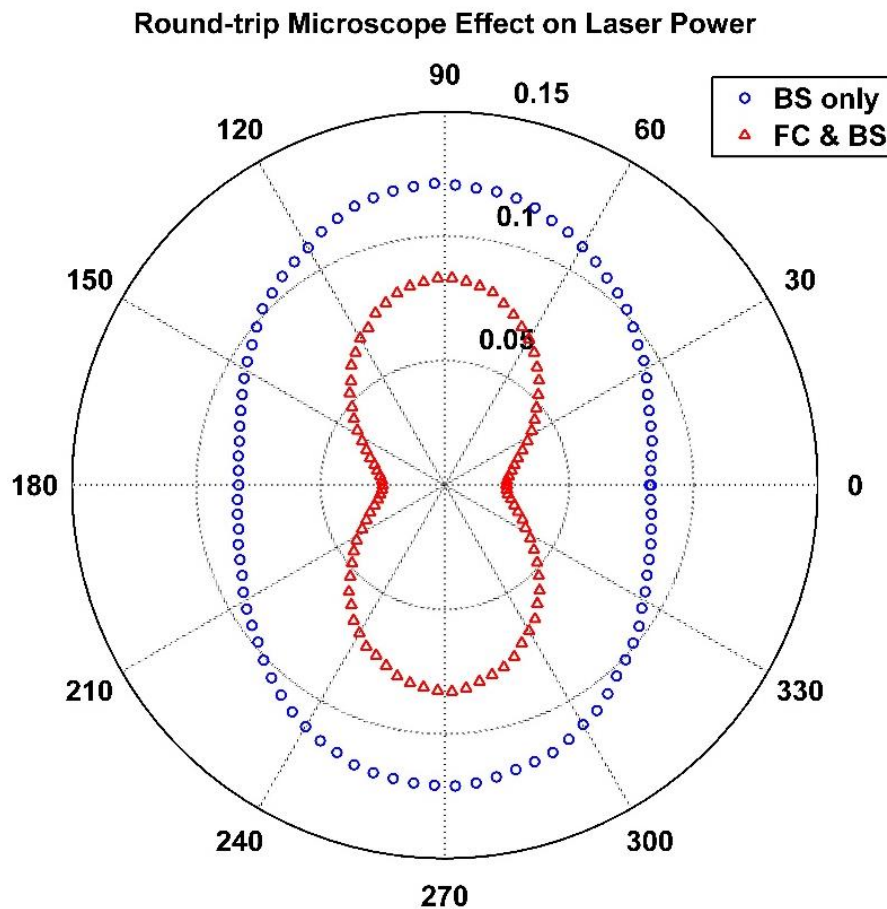


**Figure 4.11** Microscope output laser power depending on a full $360\,°$ range of laser polarization angles in round-trip path. Round-trip microscope effect shows a significant output power difference between perpendicular and parallel (to table surface) input laser polarizations.

# 4.5    Peak Amplitude Correction for Microscope Effects

As discussed in Section 4.4, the laser power transmitted through the microscope (filter cube and beamsplitter) depends on its polarization state. This microscope effect couples two variables, the laser polarization and power, making it difficult to explain which factor causes the variation of resonance peak amplitude. Hence, in order to clarify the relationship between laser polarization and nanowire resonance peak amplitude, the amplitude must be corrected for the polarization-dependent laser power variation due to the microscope.

From Figure 4.8a, we know that resonance peak amplitude $A$ is proportional to the input laser power $P_i$,

$$A \propto P_i \tag{4.12}$$

or

$$A = cP_i \tag{4.13}$$

where coefficient $c$ is a constant possessing the unit of volt per watt of input power. Here we introduce a dimensionless factor which we call the polarization effect factor, $\alpha$. The measured resonance peak amplitude $A(\alpha)$ as a function of polarization effect factor is given as

$$A(\alpha) = cP_i \cdot \alpha \tag{4.14}$$

Considering the microscope effect, polarization-dependent transmittance $T$ of the microscope optics, the measured resonance peak amplitude $A(\alpha,T)$ as a function of both polarization effect factor and transmittance can be written as

$$A(\alpha,T) = cP_i \cdot T \cdot \alpha \tag{4.15}$$

Polarization effect factor is then calculated by

$$\alpha = \frac{A(\alpha,T)}{cP_iT} \tag{4.16}$$

In the polarization test, input power $P_i$ (laser power enters the microscope) remains unchanged, so term "$cP_i$" is a constant that will not affect the variation of $\alpha$ with plane of laser polarization, though the magnitude depends on $cP_i$. Therefore Equation 4.16 can be simplified as

$$\alpha = \frac{A(\alpha,T)_{measured}}{T} \tag{4.17}$$

where $A(\alpha,T)$ is the resonance peak amplitude measured in polarization test which contains the microscope effect. $T$ is the microscope effect measured in Section 4.4. Its value varies from the microscope setup, depending on whether only the beam splitter installed (BS only) or whether both filter cube and beam splitter were installed (FC and BS). The effect of a round-trip through the microscope should be used to correct the data since in both the polarization test and the round-trip effect test, the output laser power is measured at position 3 in Figure 4.9.

**Polarization Effect on SiNW Resonance Peak Amplitude After Correction**
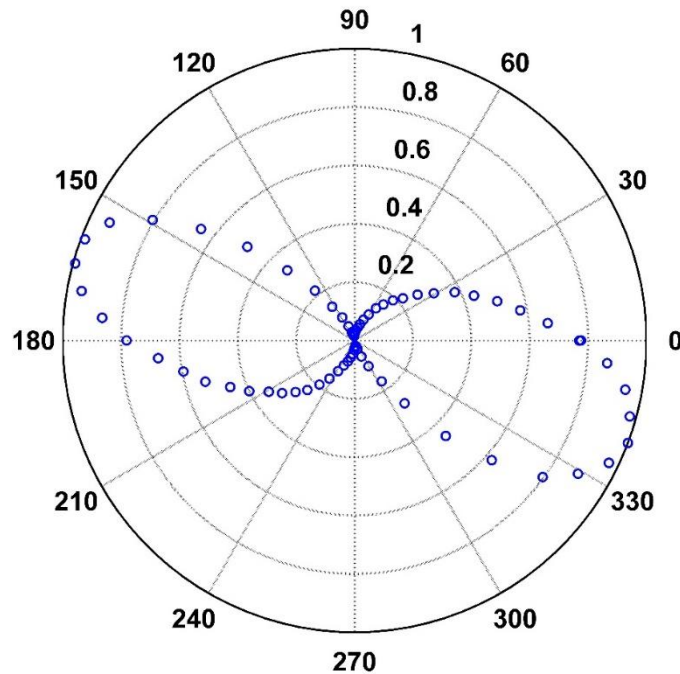


**Figure 4.12** Polar plot of polarization effect factor $\alpha$ of SiNW after correction with round-trip microscope effect (FC and BS installed) in a full range of orientation angles. Minimum $\alpha$ is obtained at 90° and 270° orientation angles (laser polarized perpendicular to the nanowire axis) which makes the resonance peak amplitude only 3% of the maximum.

In Section 4.2, normalized resonance peak amplitude of SiNW as a function of orientation angles has been presented (see Figure 4.5). However, since that data does not consider the microscope's effect on polarization, correction is required to eliminate the

influence of the microscope. Figure 4.12 illustrates the polarization effect factor $\alpha$ after correction using Equation 4.17. Nearly 97% signal amplitude degradation compared to the maximum amplitude occurs at 90 ° and 270 ° orientation angles (laser polarization is perpendicular to the nanowire axis). The maximum resonance peak amplitude is achieved when orientation angle is 0 ° or 180 ° before correction (see Figure 4.5). However, after correction, maximum polarization effect is no longer obtained by exactly setting laser polarization parallel to nanowire axis (see Figure 4.12).

## 4.6 Polarization-sensitive Resonance Peak Amplitude of Rhodium Nanowire Resonator

Inspired by the discovery of laser-nanowire interaction on a SiNW and the fact that most researchers are working on silicon resonators, it is valuable to study and verify whether the same phenomenon could be found for a metal nanowire resonator. Rhodium nanowire (RhNW) resonators fabricated in our laboratory offer a good opportunity to investigate light-matter interaction for a metal nanowire.

The experimental setup introduced in Section 3.1 was employed in studying laser-nanowire interaction on RhNW A-21 and RhNW E-76. Orientation angle θ between laser polarization and nanowire axis is adjusted by rotating the half-wavelength plate. Resonance spectrum was measured at intervals of 5 ° rotation of half-wavelength plate. An averaging over ten spectra was used to smooth the data and record a correct peak center frequency. The microscope filter cube was removed during the measurements. Raw measured data (blue circle) and corrected data (red triangle) are plotted in Figure 4.13. The correction is performed on original measurement results with round-trip microscope effect.

In Figure 4.13a and 4.13c, measured normalized peak amplitude raw data has a slight deviation from 90 ° 270 ° line. As discussed in Section 4.3, the presence of polarization-sensitive transmittance of filter cube could bring uncertainty in evaluation of the pure polarization effect on resonance peak amplitude. Therefore, correction is required to eliminate the influence of filter cube. The corrected data shows a perfect

symmetry on 90 °-270 ° line, which indicates that under TE polarization (perpendicular orientation state, 90 ° and 270 ), peak amplitude shows maximum while under TM polarization (parallel orientation state, 0 °and 180 ), the peak amplitude is minimum. The amplitude difference was found to be as much as 70% for RhNW A-21 and 78% for RhNW E-76. The tolerance of this result is ±5 °from half-wave plate rotation angle step. Using this step size instead of a smaller value is a compromise choice for decreasing total measurement time over the full 360° range of orientation angles. The laser spot drifts off the nanowire tip over longer times, limiting the total experimental time.
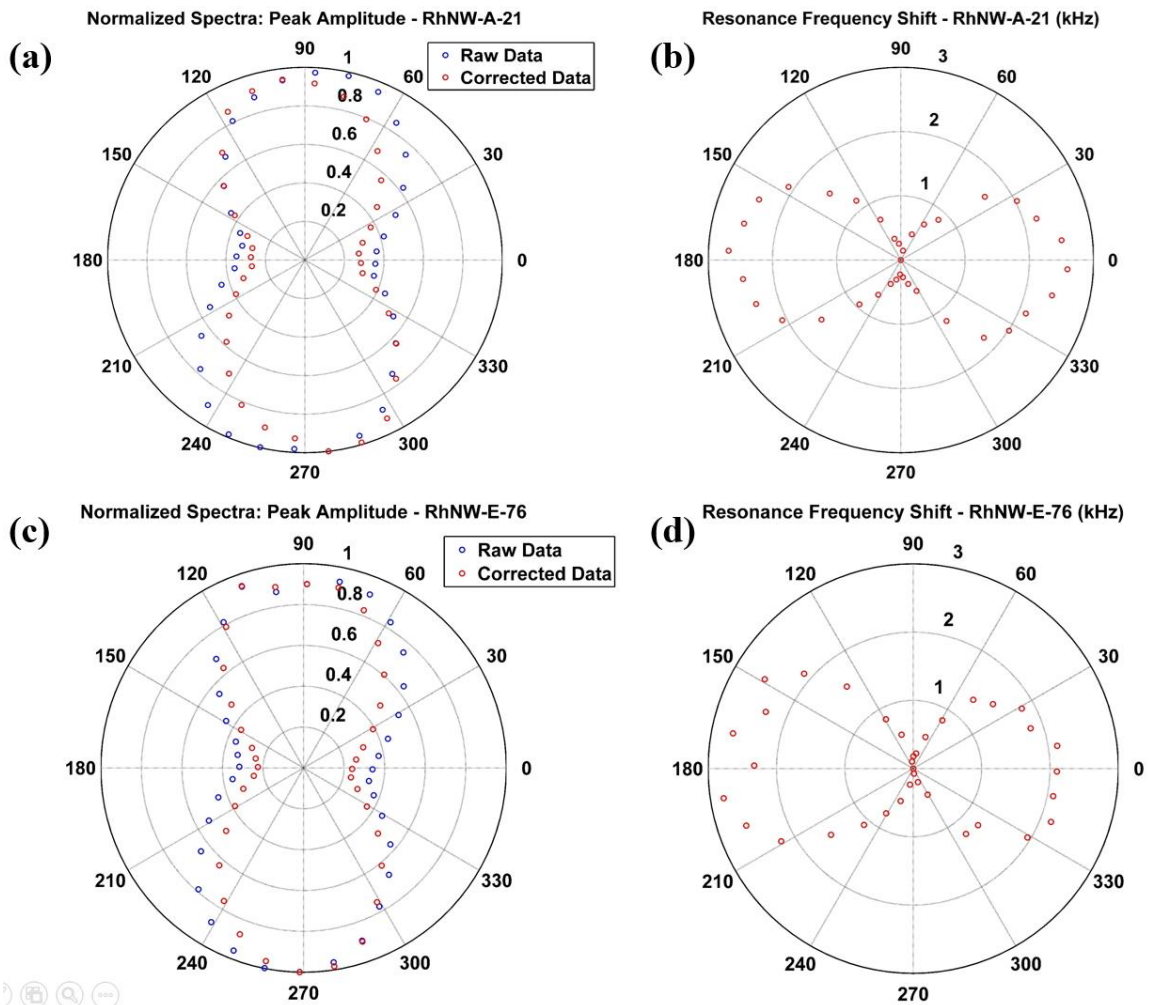


**Figure 4.13** a) Normalized resonance peak amplitude for a 360-degree range of orientation angles of RhNW A-21. Blue circles represent measured data without the filter cube installed. Amplitude data shown in red circles is a correction of the round-trip microscope effect applied to the blue circle data. b) Plots of resonance frequency shift, in kHz, at different orientation angles of RhNW A-21. The shift of resonance frequency

obtained by calculating frequency difference from the minimum resonance frequency. In the plots, zero frequency shift points represent the minimum resonance frequencies. At those zero shift points, the laser polarization is perpendicular to the nanowire axis. When the laser is polarized almost parallel to nanowire (0 ° or 180 °), resonance frequency shift reaches its maximum value. c) Normalized resonance peak amplitude for a 360-degree regime of orientation angles of RhNW E-76. d) Plots of Resonance frequency shift in kHz at different orientation angles of RhNW E-76.

As other examples of effects of polarization dependence phenomena for nanowires, the Lieber group observed the photoluminescence intensity of indium phosphide (InP) nanowire would switch from "off" to "on" as the excitation light polarization rotates from perpendicular to parallel to the nanowire axis [74]. Absorption efficiency of germanium (Ge) nanowires as optoelectronic devices was found related to the linear polarization applied, transverse-electric (TE) or transverse-magnetic (TM) [75]. Such dependence of optical absorption, emission, luminescence and photoconductivity on light polarization in semiconducting and metallic nanowires has been explained by Ruda et al. with the confined electromagnetic field induced by dielectric constants mismatch between nanowire and environment [76, 77]. Nichol et al. demonstrated a huge enhancement of signal amplitude on detected displacement of SiNWs for laser polarized parallel to the nanowire axis as compared to perpendicular in fiber-optical interferometry [69]. Also with SiNWs, Ramos and colleagues showed that scattering efficiency is a combined effect of nanowire diameter, optical polarization and the excited confined electromagnetic field inside the nanowire [78]. The confined electromagnetic field could extend out of small nanowires and interact strongly with the surrounding laser field, which affects the reflectivity amplitude of the nanowire. Field distribution of nanowire plasmons was presented to be controlled by the polarization angle on silver nanowire as well [79]. The variation of resonance peak amplitude on our RhNW is possibly an outcome of laser excitation effect depending on which polarization state is applied. Excited RhNW under parallel laser polarization tends to interact with laser beam more strongly than other polarization angles. Such intensive coupling might result in a maximum resonance peak signal amplitude. Light-nanowire interaction is still an active area of research with several unanswered questions –one of these being the relation of resonance frequency

shift with laser polarization, which appears not to have been addressed at all, to the best of our knowledge.

The resonance spectrum recorded in this laser polarization experiment not only indicates the resonance peak amplitude change but also the peak frequency change (see Figure 4.13b and 4.13d). In each experiment, there is a minimum resonance frequency and the shift is determined by the resonance frequency difference from that minimum value. In the plots, the zero frequency shift point representing the minimum resonance frequency occurs when the laser polarization is perpendicular to the nanowire axis (90° or 270°). Frequency shifts to its highest value as the laser is polarized almost parallel to nanowire in experiments. The resonance frequency shift in the polarization experiment is a complicated phenomenon that is likely caused by many factors. First, due to the microscope effect, the laser power hitting RhNW changes with input laser polarization. As described in Section 4.3, heating due to laser power absorption by the nanowire can reduce its Young's modulus value, resulting in the resonance frequency change. Second, the resonance peak amplitude variation induced by laser polarization indicates the power scattered back from nanowire changes. The difference in power absorption by the nanowire could also vary with angle of plane of polarization with respect to the nanowire.

Comparing normalized peak amplitude and resonance frequency shift results of RhNW with SiNW presented in Section 4.2, the polarization state for maximum amplitude and frequency are completely opposite. Different polarization behaviours between single-crystal semiconductor SiNW and fine-grained metal RhNW remain to be answered in the future research.

## 4.7    Summary and Outlook

The interaction between laser and nanowire resonator is investigated in terms of laser power and plane of polarization. Optical transduction method is employed to obtain the resonance frequency spectrum. The experimental data showing the resonance frequency shift and resonance peak amplitude variation induced by changing of laser power and polarization are noteworthy.

With different laser power used, the resonance frequency of RhNW resonator shifts correspondingly. Resonance frequency decreases linearly with the increase in laser power. The decrease in Young's modulus with laser power, is likely the result of heating and is measured by the shift in resonance frequency.

The filter cube and beam splitter inside the microscope were found to be polarization-sensitive. Therefore the laser power output from objective lens changes with the polarization angle of the laser beam that enters the microscope. This influence must be corrected for, in studying the relation between laser polarization and resultant resonance peak amplitude, since resonance peak amplitude linearly increases with input laser power.

Resonance peak amplitude data was recorded with varying orientation angles for the plane of laser polarization with respect to the nanowire axis ($0^\circ$). The raw data was corrected for polarization-dependent microscope effect before analysis. The corrected data shows significant dependence of resonance peak amplitude on laser polarization. Laser polarized perpendicular to the nanowire axis boosts the signal amplitude to its maximum on RhNW while laser polarized parallel to nanowire axis results in a minimum amplitude. In contrast, the SiNW showed a maximum amplitude and minimum frequency with laser polarized parallel to the nanowire axis. Furthermore, for the RhNW, the resonance peak amplitude from perpendicular to parallel was approximately tripled.

In future work, either replacing polarization-dependent components in the microscope or customizing a polarization-independent laser focusing system could be helpful in directly studying the effect of laser polarization on resonance peak amplitude. A more mechanically stable platform for nanowire resonators will allow a more accurate measurement on a full range of laser polarization angles.

# Chapter 5

# Conclusions and Future Work

This thesis investigates and clarifies the role of electrodeposited metal clamps for nanowire resonators made by field-directed assembly. It also presents data which raises new questions about laser-nanowire interaction. Resonance frequency measurement is central to mass sensing or to mechanical property measurement. Ideally, these should solely depend on the nanowire without influence of nanowire resonator structure or measurement method. However, the errors introduced by clamp and probing laser are usually omitted in traditional research. In this thesis, we have shown the extent to which clamp compliance could lower the resonance frequency compared to prediction from simple beam theory. Laser-nanowire interaction can also significantly modify the nanowire resonance peak frequency and amplitude.

It is difficult to experimentally create and study a large variety of clamp defects and conditions. To overcome this difficulty, COMSOL simulation models were created to systematically study the resonance frequency of the nanowire resonator under different clamping conditions. We also demonstrate the influence of plane of polarization and laser power on resonance spectra, during optical transduction of nanowire resonance.

The main contributions of this thesis work are listed below:

1. Our simulation results quantify the reduction in resonance frequency from the theoretical value due to compliant clamp material. A "minimum clamped depth" is defined and evaluated; resonance frequencies above this minimum value are unaffected by increasing clamped depth. Resonance frequency deviations increase as

clamped depth decreases below this minimum depth. High stiffness clamp materials like nanocrystalline diamond can provide a more rigid clamp than soft materials like gold or silver, resulting in a higher resonance frequency. This result also points to the errors caused if Euler-Bernoulli beam theory is used to calculate nanowire Young's modulus.

2. Analysis of obliquely clamped nanowires shows that the difference in resonance frequency associated with the two orthogonal vibration modes becomes larger as oblique angle increases. Defects at the clamp interface, equivalent to an asymmetric clamping condition, also causes a split into two modes -a fast and a slow mode. To the best of our knowledge, this simulation result is the first study to explain these clamp effects on two-dimensional vibrations of nanowire resonators.

3. Experimental data proves the variation of input laser power can result in a shift of the nanowire resonance peak frequency. Temperature-dependent Young's modulus under the heating of laser could explain the frequency shift. If so, the derived relation between input power and Young's modulus could provide an estimate of temperature change of the nanowire.

4. The amplitude and frequency of the resonance peak were found to be polarization -sensitive. With plane of laser polarization parallel to the RhNW axis, the resonance amplitude shows a minimum value but the resonance frequency shows a maximum value. If the laser is polarized perpendicular to the NW-axis, the maximum amplitude and minimum resonance frequency are obtained. In contrast, for the SiNW, the amplitude and frequency show maxima for polarization plane parallel and perpendicular to NW axis, respectively.

5. In the optical transduction setup, the transmittance of the filter cube and beam splitter inside the microscope were found to be polarization-dependent. This effect of the microscope causes variation in the laser power reaching the nanowire with different polarization states and should be corrected in evaluation of the polarization effect on resonance peak amplitude. One such correction method is proposed in this thesis.

This study raises several new questions that may be addressed in future work. The investigations that would be useful to pursue are listed below in order of priority:

Although the laser polarization effect has been demonstrated to have influence on nanowire resonance peak amplitude and resonance frequency, its underlying mechanism remains to be discovered. The confined electromagnetic field within a nanowire excited by different laser polarization is worth studying, since its interaction with the electromagnetic field outside the nanowire can modify the scattering efficiency. Polarization experiments should also be carried out on a variety of semiconducting and metallic nanowires to verify the extent of the difference between the two.

In the experiment, the polarization-sensitive components in the microscope cause difficulties in evaluation of the relation between laser polarization and resonance peak amplitude (and resonance frequency) of the nanowire. Improvement or modification in the optical transduction setup that remove such unwanted effects, such as introducing a circularly polarized laser beam, may help in the determination of polarization effects without the influence of laser power.

Laser heating effect could explain the resonance frequency shift in our results. However, direct evidence is needed to study the effect of temperature change on resonance frequency. By incorporating a temperature control unit to adjust the temperature of nanowire and its ambient environment, nanowire resonance frequency can be obtained over a range of temperature. This would also help to address the question of the temperature dependence of Young's modulus for the nanowires.

# Bibliography

[1]    E. Garnett and P. Yang, "Light trapping in silicon nanowire solar cells," *Nano Lett.*, vol. 10, no. 3, pp. 1082–1087, 2010.

[2]    B. Tian, X. Zheng, T. J. Kempa, Y. Fang, N. Yu, G. Yu, J. Huang, and C. M. Lieber, "Coaxial silicon nanowires as solar cells and nanoelectronic power sources," *Nature*, vol. 449, no. October, pp. 885–889, 2007.

[3]    M. Law, L. E. Greene, J. C. Johnson, R. Saykally, and P. D. Yang, "Nanowire dye-sensitized solar cells," *Nat. Mater.*, vol. 4, no. 6, pp. 455–459, 2005.

[4]    J. B. K. Law and J. T. L. Thong, "Simple fabrication of a ZnO nanowire photodetector with a fast photoresponse time," *Appl. Phys. Lett.*, vol. 88, no. 13, pp. 13–16, 2006.

[5]    H. Kind, H. Yan, B. Messer, M. Law, and P. Yang, "Nanowire ultraviolet photodetectors and optical switches," *Adv. Mater.*, vol. 14, no. 2, pp. 158–160, 2002.

[6]    J. C. Johnson, H.-J. Choi, K. P. Knutsen, R. D. Schaller, P. Yang, and R. J. Saykally, "Single gallium nitride nanowire lasers.," *Nat. Mater.*, vol. 1, no. 2, pp. 106–110, 2002.

[7]    X. Duan, Y. Huang, R. Agarwal, C. M. C. M. Lieber, and C. G. Fast, "Single-nanowire electrically driven lasers," *Nature*, vol. 421, no. 6920, pp. 241–245, 2003.

[8]    Y. Cui, "Functional Nanoscale Electronic Devices Assembled Using Silicon Nanowire Building Blocks," *Science*, vol. 291, no. 5505, pp. 851–853, 2001.

[9]    Y. Cui, Z. Zhong, D. Wang, W. U. Wang, and C. M. Lieber, "High performance silicon nanowire field effect transistors," *Nano Lett.*, vol. 3, no. 2, pp. 149–152, 2003.

[10]   Z. Fan and J. G. Lu, "Chemical sensing with ZnO nanowire field-effect transistor," *IEEE Trans. Nanotechnol.*, vol. 5, no. 4, pp. 393–396, 2006.

[11]   C. Li, D. Zhang, X. Liu, S. Han, T. Tang, J. Han, and C. Zhou, "In$_2$O$_3$ nanowires as chemical sensors," *Appl. Phys. Lett.*, vol. 82, no. 10, pp. 1613–1615, 2003.

[12]   Y. Cui, Q. Wei, H. Park, and C. M. Lieber, "Nanowire Nanosensors for Highly Sensitive and Selective Detection of Biological and Chemical Species," *Science*, vol. 293, no. 5533, pp. 1289–1292, 2001.

[13]   G. Zheng, F. Patolsky, Y. Cui, W. U. Wang, and C. M. Lieber, "Multiplexed electrical detection of cancer markers with nanowire sensor arrays," *Nat. Biotechnol.*, vol. 23, no. 10, pp. 1294–1301, 2005.

[14]   J. Hahm and C. M. Lieber, "Direct ultrasensitive electrical detection of DNA and DNA sequence variations using nanowire nanosensors," *Nano Lett.*, vol. 4, no. 1, pp. 51–54, 2004.

[15]   M. Curreli, R. Zhang, F. N. Ishikawa, H. K. Chang, R. J. Cote, C. Zhou, and M. E. Thompson, "Real-time, label-free detection of biological entities using nanowire-based FETs," *IEEE Trans. Nanotechnol.*, vol. 7, no. 6, pp. 651–667, 2008.

[16]   Z. L. Wang, "Piezoelectric Nanogenerators Based on Zinc Oxide Nanowire Arrays," *Science*, vol. 312, no. 5771, pp. 242–246, 2006.

[17] R. B. Bhiladvala, "Nanomechanical Resonant Sensors and Fluid Interactions," in *Encyclopedia of Nanotechnology*, Springer, 2012, pp. 1630–1643.

[18] K. Hess and G. J. Iafrate, "Approaching the quantum limit," *IEEE Spectr.*, vol. 29, no. 7, pp. 44–49, 1992.

[19] A. N. Cleland, M. Pophristic, and I. Ferguson, "Single-crystal aluminum nitride nanomechanical resonators," *Appl. Phys. Lett.*, vol. 79, no. 13, pp. 2070–2072, 2001.

[20] C. Li and T. W. Chou, "Single-walled carbon nanotubes as ultrahigh frequency nanomechanical resonators," *Phys. Rev. B*, vol. 68, no. 7, pp. 1–3, 2003.

[21] C. Li and T. W. Chou, "Vibrational behaviors of multiwalled carbon nanotube based nanomechanical resonators," *Appl. Phys. Lett.*, vol. 84, no. 1, pp. 121–123, 2004.

[22] A. Husain, J. Hone, H. W. C. Postma, X. M. H. Huang, T. Drake, M. Barbic, A. Scherer, and M. L. Roukes, "Nanowire-based very-high-frequency electromechanical resonator," *Appl. Phys. Lett.*, vol. 83, no. 6, p. 1240, 2003.

[23] X. L. Feng, R. He, P. Yang, and M. L. Roukes, "Very high frequency silicon nanowire electromechanical resonators," *Nano Lett.*, vol. 7, no. 7, pp. 1953–1959, 2007.

[24] N. A. Melosh, "Ultra-high density nanowire lattices and circuits," *Science*, vol. 300, no. 2003, pp. 112–115, 2003.

[25] K. C. Schwab and M. L. Roukes, "Putting Mechanics into Quantum Mechanics," *Phys. Today*, no. July, pp. 36–42, 2005.

[26] J. A. Sioss, R. B. Bhiladvala, W. Pan, M. Li, S. Patrick, P. Xin, S. L. Dean, C. D. Keating, T. S. Mayer, and G. A. Clawson, "Nanoresonator chip-based RNA sensor strategy for detection of circulating tumor cells: Response using PCA3 as a prostate cancer marker," *Nanomedicine Nanotechnology, Biol. Med.*, vol. 8, no. 6, pp. 1017–1025, 2012.

[27] P. Paulitschke, N. Seltner, a. Lebedev, H. Lorenz, and E. M. Weig, "Size-independent Young's modulus of inverted conical GaAs nanowire resonators," *Appl. Phys. Lett.*, vol. 103, no. 26, p. 261901, Dec. 2013.

[28] R. B. Bhiladvala and Z. J. Wang, "Effect of fluids on the Q factor and resonance frequency of oscillating micrometer and nanometer scale beams," *Phys. Rev. E - Stat. Nonlinear, Soft Matter Phys.*, vol. 69, no. 3 2, pp. 1–5, 2004.

[29] A. Boisen, S. Dohn, S. S. Keller, S. Schmid, and M. Tenje, "Cantilever-like micromechanical sensors," *Reports Prog. Phys.*, vol. 74, no. 3, p. 036101, Mar. 2011.

[30] J. Chaste, A. Eichler, J. Moser, G. Ceballos, R. Rurali, and A. Bachtold, "A nanomechanical mass sensor with yoctogram resolution," *Nat. Nanotechnol.*, vol. 7, no. 5, pp. 301–304, 2012.

[31] K. L. Ekinci, "Electromechanical transducers at the nanoscale: Actuation and sensing of motion in nanoelectromechanical systems (NEMS)," *Small*, vol. 1, no. 8–9, pp. 786–797, 2005.

[32] S. C. Jun, H. Son, C. W. Baik, J. M. Kim, S. W. Moon, H. J. Kim, X. M. H. Huang, and J. Hone, "Electrothermal noise analysis in frequency tuning of nanoresonators," *Solid. State. Electron.*, vol. 52, no. 9, pp. 1388–1393, 2008.

[33]    A. N. Cleland and M. L. Roukes, "Fabrication of high frequency nanometer scale mechanical resonators from bulk Si crystals," *Appl. Phys. Lett.*, vol. 69, no. 18, pp. 2653–2655, 1996.

[34]    X. M. H. Huang, C. A. Zorman, M. Mehregany, and M. L. Roukes, "Nanodevice motion at microwave frequencies," *Nature*, vol. 421, no. January, pp. 496–497, 2003.

[35]    N. Sinha, G. E. Wabiszewski, R. Mahameed, V. V. Felmetsger, S. M. Tanner, R. W. Carpick, and G. Piazza, "Piezoelectric aluminum nitride nanoelectromechanical actuators," *Appl. Phys. Lett.*, vol. 95, no. 5, 2009.

[36]    S. C. Masmanidis, R. B. Karabalin, I. De Vlaminck, G. Borghs, M. R. Freeman, and M. L. Roukes, "Multifunctional nanomechanical systems via tunably coupled piezoelectric actuation.," *Science*, vol. 317, no. 5839, pp. 780–783, 2007.

[37]    M. A. Haque and M. T. A. Saif, "Application of MEMS force sensors for in situ mechanical characterization of nano-scale thin films in SEM and TEM," *Sensors Actuators, A Phys.*, vol. 97–98, pp. 239–245, 2002.

[38]    R. C. Batra, M. Porfiri, and D. Spinello, "Review of modeling electrostatically actuated microelectromechanical systems," *Smart Mater. Struct.*, vol. 16, no. 6, pp. R23–R31, 2007.

[39]    E. Forsen, G. Abadal, S. Ghatnekar-Nilsson, J. Teva, J. Verd, R. Sandberg, W. Svendsen, F. Perez-Murano, J. Esteve, E. Figueras, F. Campabadal, L. Montelius, N. Barniol, and A. Boisen, "Ultrasensitive mass sensor fully integrated with complementary metal-oxide-semiconductor circuitry," *Appl. Phys. Lett.*, vol. 87, no. 4, pp. 2003–2006, 2005.

[40]  D. a. Dikin, X. Chen, W. Ding, G. Wagner, and R. S. Ruoff, "Resonance vibration of amorphous $SiO_2$ nanowires driven by mechanical or electrical field excitation," *J. Appl. Phys.*, vol. 93, no. 1, p. 226, 2003.

[41]  R. S. Ruoff, D. Qian, and W. K. Liu, "Mechanical properties of carbon nanotubes: Theoretical predictions and experimental measurements," *Comptes Rendus Phys.*, vol. 4, no. 9, pp. 993–1008, 2003.

[42]  M. F. Yu, G. Wagner, R. Ruoff, and M. Dyer, "Realization of parametric resonances in a nanowire mechanical system with nanomanipulation inside a scanning electron microscope," *Phys. Rev. B*, vol. 66, no. 7, pp. 1–4, 2002.

[43]  R. B. Karabalin, X. L. Feng, and M. L. Roukes, "Amplification at Very High Frequency," *Nano Lett.*, vol. 9, no. 9, pp. 3116-3123, 2009.

[44]  S. Ghatnekar-Nilsson, E. Forsén, G. Abadal, J. Verd, F. Campabadal, F. Pérez-Murano, J. Esteve, N. Barniol, a Boisen, and L. Montelius, "Resonators with integrated CMOS circuitry for mass sensing applications, fabricated by electron beam lithography," *Nanotechnology*, vol. 16, no. 1, pp. 98–102, 2004.

[45]  T. Kouh, D. Karabacak, D. H. Kim, and K. L. Ekinci, "Diffraction effects in optical interferometric displacement detection in nanoelectromechanical systems," *Appl. Phys. Lett.*, vol. 86, no. 1, p. 013106, 2005.

[46]  I. Favero and K. Karrai, "Optomechanics of deformable optical cavities," *Nat. Photonics*, vol. 3, no. 4, pp. 201–205, Apr. 2009.

[47]  D. W. Carr, S. Evoy, L. Sekaric, H. G. Craighead, and J. M. Parpia, "Measurement of mechanical resonance and losses in nanometer scale silicon wires," *Appl. Phys. Lett.*, vol. 75, no. 7, pp. 920–922, 1999.

[48] C. O'Mahony, M. Hill, P. J. Hughes, and W. A. Lane, "Titanium as a micromechanical material," *J. Micromechanics Microengineering*, vol. 12, pp. 438–443, 2002.

[49] M. Sam, N. Moghimian, and R. B. Bhiladvala, "Field-directed assembly of nanowires: identifying directors, disruptors and indices to maximize the device yield," *Nanoscale*, vol. 8, no. 2, pp. 889–900, 2016.

[50] P. Poncharal, Z. L. Wang, D. Ugarte, W. A. de Heer, and W. De Heer, "Electrostatic deflections and electromechanical resonances of carbon nanotubes," *Science*, vol. 283, no. 5407, pp. 1513–1516, 1999.

[51] W. Weaver, S. Timoshenko, and D. H. . Young, *Vibration Problems in Engineering*, 5th ed. Wiley-Interscience, 1990.

[52] W. Ding, L. Calabri, X. Chen, K. M. Kohlhaas, and R. S. Ruoff, "Mechanics of crystalline boron nanowires," *Compos. Sci. Technol.*, vol. 66, no. 9, pp. 1112–1124, Jul. 2006.

[53] L. Calabri, N. Pugno, W. Ding, and R. S. Ruoff, "Resonance of curved nanowires," *J. Phys. Condens. Matter*, vol. 18, no. 33, pp. S2175–S2183, Aug. 2006.

[54] Q. Qin, F. Xu, Y. Cao, P. I. Ro, and Y. Zhu, "Measuring true Young's modulus of a cantilevered nanowire: effect of clamping on resonance frequency.," *Small*, vol. 8, no. 16, pp. 2571–2576, Aug. 2012.

[55] K. E. Spear and J. P. Dismukes, *Synthetic diamond: Emerging CVD science and technology*. Wiley, 1994.

[56] K. F. Murphy, L. Y. Chen, and D. S. Gianola, "Effect of organometallic clamp properties on the apparent diversity of tensile response of nanowires.," *Nanotechnology*, vol. 24, no. 23, p. 235704, Jun. 2013.

[57] X. Chen, "Mechanical resonance of quartz microfibers and boundary condition effects," *J. Appl. Phys.*, vol. 95, no. 9, p. 4823, 2004.

[58] D. J. Zeng and Q. S. Zheng, "Resonant frequency-based method for measuring the Young's moduli of nanowires," *Phys. Rev. B*, vol. 76, no. 7, p. 075417, Aug. 2007.

[59] D. Zeng, X. Wei, J. Z. Liu, Q. Chen, X. Li, and Q. Zheng, "Tunable resonant frequencies for determining Young's moduli of nanowires," *J. Appl. Phys.*, vol. 105, no. 11, p. 114311, 2009.

[60] D. W. Carr, L. Sekaric, and H. G. Craighead, "Measurement of nanomechanical resonant structures in single-crystal silicon," *J. Vac. Sci. Technol. B Microelectron. Nanom. Struct.*, vol. 16, no. 6, p. 3821, Nov. 1998.

[61] K. L. Ekinci, "Ultimate limits to inertial mass sensing based upon nanoelectromechanical systems," *J. Appl. Phys.*, vol. 95, no. 5, p. 2682, 2004.

[62] M. Belov, N. J. Quitoriano, S. Sharma, W. K. Hiebert, T. I. Kamins, and S. Evoy, "Mechanical resonance of clamped silicon nanowires measured by optical interferometry," *J. Appl. Phys.*, vol. 103, no. 7, p. 074304, 2008.

[63] N. Moghimian, "Electrochemical control for nanoelectromechanical device production," PhD dissertation, Univeristy of Victoria, 2015.

[64] M. Sam, "Controlling field-directed assembly of nanowires: towards nanomanufacturing for biosensors and transparent electrodes," PhD dissertation, University of Victoria, 2015.

[65]  M. Li, "Hybrid integration of nanowire resonator arrays," PhD dissertation, Pennsylvania State University, 2008.

[66]  H. Kuhn and D. Medlin, *ASM Handbook Volume 8:Mechanical testing and evaluation*. 2000.

[67]  M. Li, T. S. Mayer, J. A. Sioss, C. D. Keating, and R. B. Bhiladvala, "Template-grown metal nanowires as resonators: performance and characterization of dissipative and elastic properties.," *Nano Lett.*, vol. 7, no. 11, pp. 3281–3284, Nov. 2007.

[68]  F. Aguilar Sandoval, M. Geitner, É. Bertin, and L. Bellon, "Resonance frequency shift of strongly heated micro-cantilevers," *J. Appl. Phys.*, vol. 117, no. 23, p. 234503, 2015.

[69]  J. M. Nichol and R. Budakian, "Displacement detection of silicon nanowires by polarization-enhanced fiber-optic interferometry," *Appl. Phys. Lett.*, vol. 93, no. 19, p. 193110, 2008.

[70]  J. Merker, D. Lupton, M. Topfer, and H. Knake, "High Temperature Mechanical Properties of the Platinum Group Metals," *Platin. Met. Rev.*, vol. 45, no. 2, pp. 74–82, 2001.

[71]  V. Pini, J. Tamayo, E. Gil-Santos, D. Ramos, P. Kosaka, H. Tong, C. van Rijn, and M. Calleja, "Shedding Light on Axial Stress Effect on Resonance Frequencies of Nanocantilevers," *ACS Nano*, vol. 5, no. 6, pp. 4269–4275, Jun. 2011.

[72]  E. Gil-Santos, D. Ramos, V. Pini, J. Llorens, M. Fernández-Regúlez, M. Calleja, J. Tamayo, and  a San Paulo, "Optical back-action in silicon nanowire resonators:

bolometric versus radiation pressure effects," *New J. Phys.*, vol. 15, no. 3, p. 035001, Mar. 2013.

[73] Z. Y. Zhong, W. M. Zhang, G. Meng, and M. Y. Wang, "Thermoelastic damping in optical waveguide resonators with the bolometric effect," *Phys. Rev. E*, vol. 89, no. 6, p. 063203, Jun. 2014.

[74] J. Wang and C. Lieber, "Highly polarized photoluminescence and photodetection from single indium phosphide nanowires.," *Science*, vol. 293, no. 5534, pp. 1455–1457, Aug. 2001.

[75] L. Cao and M. L. Brongersma, "Engineering light absorption in semiconductor nanowire devices.," *Nat. Mater.*, vol. 8, no. 8, pp. 643–647, Aug. 2009.

[76] H. E. Ruda and A. Shik, "Polarization-sensitive optical phenomena in thick semiconducting nanowires," *J. Appl. Phys.*, vol. 100, no. 2, p. 024314, 2006.

[77] H. E. Ruda and A. Shik, "Polarization-sensitive optical phenomena in semiconducting and metallic nanowires," *Phys. Rev. B - Condens. Matter Mater. Phys.*, vol. 72, no. 11, 2005.

[78] D. Ramos, E. Gil-Santos, and J. Tamayo, "Silicon nanowires: where mechanics and optics meet at the nanoscale.," *Sci. Rep.*, vol. 3, p. 3445, Jan. 2013.

[79] H. Wei, Z. Li, X. Tian, Z. Wang, F. Cong, N. Liu, S. Zhang, P. Nordlander, N. J. Halas, and H. Xu, "Quantum dot-based local field imaging reveals plasmon-based interferometric logic in silver nanowire networks," *Nano Lett.*, vol. 11, no. 2, pp. 471–475, 2011.